Article:
Peng, R, Di, B, Glover, PWJ et al. (2020) Seismo-electric conversion in shale: experiment and analytical modelling. Geophysical Journal International, 223 (2). pp. 725-745. ISSN: 0956-540X

https://doi.org/10.1093/gji/ggaa288

Geophysical Journal International

Seismo-electric conversion in shale: Experiment and analytical modelling

Journal:	*Geophysical Journal International*
Manuscript ID	GJI-19-0932.R2
Manuscript Type:	Research Paper
Date Submitted by the Author:	n/a
Complete List of Authors:	Peng, Rong; MNR Key Laboratory of Metallogeny and Mineral Assessment, Institute of Mineral Resources,CAGS; China University of Petroleum Beijing Di, Rang; China University of Petroleum Beijing Glover, P; University of Leeds, School of Earth and Environment Wei, Jianxin; China University of Petroleum, Geosciences Lorinczi, Piroska; University of Leeds, School of Earth and Environment Liu, Chu; China University of Petroleum (Beijing)
Keywords:	Numerical modelling < GEOPHYSICAL METHODS, Permeability and porosity < COMPOSITION and PHYSICAL PROPERTIES, Electromagnetic theory < GEOMAGNETISM and ELECTROMAGNETISM

Seismo-electric conversion in shale: Experiment and analytical modelling

Rong Peng[1, 2], Bangrang Di[2], Paul Glover[3], Jianxin Wei[2], Piroska Lorinczi[3], Zichun Liu[2], Huafei Li[4]*

1 MNR Key Laboratory of Metallogeny and Mineral Assessment, Institute of Mineral Resources, CAGS, Beijing, 100037, China

2 College of Geophysics and Information Engineering, China University of Petroleum (Beijing), 102249, China

3 School of Earth and Environment, University of Leeds, UK

4 Processing Center of GRI, BGP, Zhuozhou City, Hebei Province, 072750, China

Rong Peng: hnpengrong@163.com

Bangrang Di: cupdbr@126.com

Paul Glover: P.W.J.Glover@leeds.ac.uk **Corresponding Author**

Jianxin Wei: weijx@cup.edu.cn

Piroska Lorinzi: P.Lorinczi@leeds.ac.uk

Zichun Liu: liuzichun111@163.com

Abstract

The development of seismo-electric exploration techniques relies critically upon the strength of the seismo-electric conversion. However, there have been very few seismo-electric measurements or modelling on shales, despite shales accounting for the majority of unconventional reservoirs. We have carried out seismo-electric measurements on Sichuan Basin shales (permeability 0.00147 – 0.107 mD), together with some comparative measurements on sandstones (permeability 0.2–60 mD). Experimental results show that the amplitudes of the seismoelectric couplingcoefficient in shales are comparable to that exhibited by sandstones, and are approximately independent of frequency in the seismic frequency range (<1 kHz). Numerical modelling has also been used to examine the effects of varying (i) dimensionless number, (ii) porosity, (iii) permeability, (iv) tortuosity, and (v) zeta potential on seismo-electric conversion in porous media. It was found that while changes in dimensionless number and permeability seem to have little effect, seismoelectric coupling coefficient is highly sensitive to changes in porosity, tortuosity and zeta potential. Numerical modelling suggests that the cause of the seismo-electric conversion in shales is enhanced zeta potentials caused by clay minerals, which are highly frequency dependent. This is supported by a comparison of our numerical modelling with our experimental data, together with an analysis of seismo-electric conversion as a function of clay mineral composition from XRD measurements. The sensitivity of seismo-electric coupling to the clay minerals suggests that seismo-electric exploration may have potential for the characterization of clay minerals in shale gas and shale oil reservoirs.

Keywords: Seismo-electric conversion, shales, frequency-dependence, porosity, permeability, tortuosity

1 Introduction

Seismo-electric conversion occurs when the passage of an elastic wave through an aqueous fluid saturated porous medium causes that fluid to move, and where the resulting fluid movement separates charge such that an electrical potential is developed across the medium (e.g., Haines et al. 2007; Glover, 2012a; 2012b). Seismo-electric effects occur in all aqueous fluid-filled porous media, including sandstones and shales. Laboratory experiments (e.g., Glover & Déry 2010; Peng et al. 2016; Schakel et al. 2011a; 2011b; Zhu et al. 2008; 2013; 2015; Wang et al. 2015a, b; 2016) of electro-kinetic and seismo-electric coupling conducted in sandstones indicate that a relative strong seismo-electric conversion can be generated in sandstones, especially when the pore fluid salinity is low (Walker & Glover 2018). Currently, there is a good and growing body of experimental measurements on sandstones, limestones, sands and glass beads. By contrast, there has been less seismo-electric research on shales. The strength of seismo-electric conversion in shales, and the parameters which control it, remain uncertain.

Thompson & Gist (1993) first presented the results of seismo-electric profiling to detect the signals generated at interfaces between high permeability water sands and low permeability shales at depths of up to 300 m. In their study, the media on each side of the interface produced a strong electric contrast as well as different rock properties, which together enhanced the seismo-electric conversion. However, the specific influences of shale on seismo-electric conversion were either not studied or were not reported. Numerical modelling of seismo-electric processes for a similar interface was carried out by Revil et al. (2015). In their study, the seismo-electric wavefield induced at the shale-sand interface during the passage of a seismic P-wave was also characterized by the difference in electrical conductivity between the shale and the sandstone layers. Meanwhile, modelling of the seismo-electric properties of a sand channel surrounded by clay (Haines & Pride 2006) and clay lenses embedded in sandstone (Kröger et al. 2009) have also indicated that the seismo-electric method can detect clay or shale interfaces as well as interbedded layers and lenses of clays and sandstones. In addition, Jougnot et al. (2010) studied the streaming potential coupling coefficient of clay rocks as a function of saturation experimentally and showed that the coupling coefficient was a power law function of the relative water saturation.

Field measurements have also suggested that electric signals induced by seismic waves through seismo-electric coupling may be used to image the subsurface boundaries of sand and clay layers (Butler et al. 1996; 2002; Thompson et al. 2007; Dupuis et al. 2009; Glover & Jackson 2010). The sparse experimental and field data suggest that shale exhibits a sizeable electric coupling coefficient. However, since no authoritative value is currently available, numerical modelling studies assume a significant electric coupling coefficient for shales.

Clay minerals are a major component of shales. They are known to have a strong impact on the hydraulic and electrical properties of rocks (e.g., Arulanandan 1969; Alali 2007; Santiwong et al. 2008). Consequently, it is expected that the fraction of clay minerals will also exert a partial control on the seismo-electric properties of shales. The processes leading to seismo-electric conversion occur in the electric double layer (EDL) (Shaw 1992; Pride 1994; Glover 2015) which forms at the solid-fluid interface in porous media. Theoretical developments (Revil & Glover 1997; 1998; Revil et al. 1999) have shown that the size of the Stern potential developed at the mineral-fluid interface depends upon the composition of the mineral grains and fluid (Leroy & Revil 2004; Tournassat et al. 2009; 2013; Leroy et al. 2015). Since the surface charge controls the Stern zeta potential, which, together with the rock microstructure, controls the streaming potential coefficient (Glover & Déry 2010; Glover 2012; Li et al. 2016), there is a functional link between clay minerals and seismoelectric coupling coefficient (Revil et al. 2005; Peng et al. 2018b). It is known that the phase due to induced polarization and Maxwell Wagner polarization (MWP) is very strong in shales (several hundreds of milliradians), which plays an important role in the seismoelectric coupling coefficient (Leroy and Revil, 2009; 2015). This effect is not accounted for in the Pride (1994) model, which was formulated for silica-based rocks. Furthermore the Pride model does not take account of the Stern Layer which can contain the majority of counterions. This creates a strong frequency dependent complex conductivity because of induced polarization. Consequently, the Pride model should be considered to represent the bottom limit of possible frequency-dependence in shales.

Another difficulty is that many of the models developed for describing both steady-state (Glover et al. 2012b; Walker & Glover 2014; 2018) or frequency-dependent (Peng et al. 2019; Glover 2018) electro-kinetic coupling measurements make the assumption that the EDL is thin compared to the pore size. This has been a restriction since the first models (Glover et al. 1994; Revil & Glover 1995) and provides difficulties for porous media with either small pores (such as shales), or medium to large pores when the pore fluid has very low salinities. In practice, the latter effect is not observed because mineral-fluid equilibrium ensures that sufficiently low salinities cannot be attained in rocks (Walker & Glover 2014). Instead, it is the pore microstructure that dominates the low salinity behaviour of streaming potential coupling (Glover et al. 2012b; 2018). The effect of the assumption is that rocks with very small pores will have their pore space dominated by the EDL, and any coupling will subsequently be limited, leading to measured coupling coefficients that are less than would have occurred if the rock had been composed of larger pores. In this work we implement a modification which allows thick double layers to be modelled (Kozak & Davis 1987).

In this paper, we present experimental measurements of seismo-electric conversion for 14 shale samples and 5 sandstone samples, the latter of which are primarily included for comparison. In addition, we have compared the differences in seismo-electric coupling between sandstones and shales by carrying out limited numerical modelling of the seismo-electric coupling as a function of

frequency using Pride's (1994) equation with no MWP and Stern Layer component. Importantly, both experimental results and modelling show that the intensity of the seismo-electric conversion in the low-permeability shale is comparable to that produced in high-permeability sandstones. However, we acknowledge that new modelling will be necessary to extend the Pride (1994) model to include Stern Layer/Maxwell-Wagner effects before the experimental measurements can be fully accounted for.

2 Theory

Coupling between the acoustic field and electromagnetic fields of porous media depends on the existence of the electric-double layer (EDL), which is formed at the solid-fluid boundary in the pore space of porous media. The EDL includes a diffuse layer, which is electrically polarised, having unequal concentrations of positive and negative ions. Only the part of the diffuse layer closest to the mineral surface will be immobile, while the remainder will remain capable of flow. The propagation of seismic waves in the fluid-filled porous media causes movement of mobile fluids relative to the solid matrix (Glover et al. 2012b). Consequently, ions in the electrically neutral bulk fluid are moved together with electrically unbalanced ions in the mobile part of the diffuse layer. The resulting separation of charge leads to the development of a streaming potential, and a streaming counter-current which flows to balance the induced charge separation. The transient current flow is capable of generating electro-magnetic waves at discontinuous boundaries. Also the seismoelectric coupling coefficient $L(\omega)$ is developed to describe the coupling between the seismic and electromagnetic fields (Pride 1994; Haartsen & Pride 1997; Haines et al. 2007; Jouniaux & Zyserman 2016).

Pride (1994) derived the governing equations of the seismo-electric conversion for saturated porous media expressing the frequency-dependent seismo-electric coupling coefficient as

$$L(\omega) = L_0\left[1 - i\frac{\omega m^*}{\omega_c\ 4}\left(1 - 2\frac{\tilde{d}}{\Lambda}\right)^2\left(1 - i^{3/2}\frac{\tilde{d}}{\delta}\right)^2\right]^{-1/2}, \quad \textbf{(1)}$$

where, L_0 is the low frequency seismo-electric coupling coefficient, δ is the skin depth, $\delta = \sqrt{\frac{\eta}{\omega\rho_f}}$, η is the pore fluid viscosity, ρ_f is the density of the pore fluid, $\tilde{d}$ is the Debye length, Λ is the characteristic length scale of the pores (Johnston et al. 1987). It should be noted that Pride model does not account for surface conductivity in the Stern layer band hence does not include induced polarization (IP) effects.

In Equation (1) the transition frequency, ω_c, separating low-frequency viscous flow and high-frequency inertial flow, is given by

$$\omega_c = \frac{\phi\eta}{\alpha_\infty \rho_f k_0}, \quad \textbf{(2)}$$

where ϕ is the porosity, k_0 is the steady-state permeability of the porous medium, and α_∞ is the tortuosity of the pore space.

The tortuosity is a term used to describe the sinuosity and interconnectedness of the pore space as it affects transport processes through porous media. Tortuosity has no simple or universal definition (Clennell 1997). We may understand the tortuosity in a simplified but not comprehensive way that the tortuosity of a pathway is defined as the ratio of the length of the pathway to the distance between the ends of it (Epstein 1989). There are many models for tortuosity estimation including hydraulic models ($\alpha_{\infty h}$), electric models ($\alpha_{\infty e}$) and diffusive models ($\alpha_{\infty d}$). Values for hydraulic electrical and diffusional tortuosity are in general different from one another. Electrical tortuosity is defined in terms of conductivity whereas hydraulic tortuosity is usually defined geometrically, and diffusional tortuosity is typically computed from temporal changes in concentration (Clennell 1997). Usually, it is considered that $\alpha_{\infty d} \approx \alpha_{\infty e} < \alpha_{\infty h}$ holds (Saomoto & Katagiri 2015; Thanh et al. 2019). In this paper, we use the α_∞ to represent tortuosity and consider $\alpha_\infty = \alpha_{\infty d} = \alpha_{\infty e}$. Another definition was made by Glover (2009) in his physical interpretation of the cementation exponent, m as the rate of change of connectedness (G) of a porous medium with porosity (ϕ) and connectivity (χ), as $m = \frac{d^2G}{d\chi d\phi}$, where the tortuosity is the inverse of the connectivity, $\alpha_{\infty e}=1/\chi$.

Each of the models for tortuosity are a function of porosity despite of the difference between their background concepts (Saomoto & Katagiri 2015). The electrical tortuosity can be expressed as $\alpha_{\infty e}= \phi^{1-m}$ (David 1993; Glover 2012), where m is the cementation exponent. We do not use this equation to obtain the tortuosity in this work because it introduces a new unknown parameter m into the calculations. Similar expressions of tortuosity exist which are based on the experimental data. Bruggeman (1935) defined $\alpha_{\infty e}=\phi^{-\alpha}$, with α usually chosen as 0.5, valid for packs of grains of porosity $\phi > 0.2$. this particular definition infers that m=1.5 for packs of glass beads, a result which has been validated. In this work we have used the modified Weissberg model (Boudreau 1996) to calculate the tortuosity

$$\alpha_\infty = \sqrt{1 - 2.02ln(\phi)} \quad . \quad \textbf{(3)}$$

This relationship is an empirical equation which shows the best least-squares fits to experimental data.

The Pride (1994) model contains a dimensionless number (m), which we relabel as m^* in order not to confuse it with the cementation exponent. The dimensionless number m^* is given by (Pride 1994; Walker & Glover 2010)

$$m^* = \frac{\phi}{\alpha_\infty k_0}\Lambda^2, \tag{4}$$

The value of m^* is assumed to be 8 for sandstones (Pride 1994), and 12 if shale is modelled as a layered porous medium (Johnson et al. 1987). It should be noted that for most geological media the pore fluid is sufficiently saline for the Debye length to be much smaller than the characteristic length scale (i.e., $\tilde{d} << \Lambda$). However, the pore size of shales may be comparable to the thickness of the double layer, hence, the thick double layer approximation have been developed. The assumption of thin double layer has been extended to account for thicker double layers, which still allows significant simplifications to be made (Kozak & Davis 1987).

The low-frequency seismoelectric coupling coefficient L_0 can be written as

$$L_0 = -\frac{\phi\,\varepsilon_f\zeta}{\alpha_\infty\,\eta}\left[1 - 2\frac{\tilde{d}}{\Lambda}\right], \tag{5}$$

where ζ is the zeta potential, $\mathcal{E}_f$ represents the fluid permittivity. If $\tilde{d} << \Lambda$, L_0 can be simplified to

$$L_0 = -\frac{\phi\,\varepsilon_f\zeta}{\alpha_\infty\,\eta}, \tag{6}$$

which is a statement of the classical Helmholtz-Smoluchowski equation (e.g., Glover 2012).

3 Experimental Measurement

3.1 Experimental Methodology

The apparatus we have used to measure seismo-electric conversion in shale is shown in Figure 1. Both the seismo-electric and acoustic signals are collected by this apparatus, which operates in a water tank (Peng et al. 2017; 2018a). A compressional wave transducer (Panametrics-NDT V101, central frequency 0.5 MHz) produces acoustic waves, which propagate across a sample (4 cm×4 cm×2 cm). These waves induce transient pressure differences across the sample, which give rise to the seismoelectric coupling in the sample.

The transient pressures at each side of the sample (P1 and P2) are measured by transient pressure transducers (also Panametrics-NDT V101), which are placed on each side of the rock sample. The

transient pressure difference ΔP (ΔP=P1-P2) is amplified by a pre-amplifier (Olympus Ultrasonic Preamplifier 5660c) and monitored using an oscilloscope (Agilent Technology DSO6012A).

The transient seismoelectric voltage signals at each side of the sample are measured by two non-polarising Ag/AgCl electrodes (V1 and V2). These electrodes cover the entirety of two opposite faces of the sample (i.e., each are 4 cm×4 cm in area) and are 0.1 cm thick. The electrodes are placed between the pressure transducers and the sample, and are positioned 0.1 cm away from the sample surface to avoid the surface conductivity in our experiments. The instantaneous seismo-electric potential ΔV is the instantaneous difference between these two potential measurements (ΔV=V1-V2).

The seismoelectric coupling coefficient $L(\omega)$ calculated by the amplitude of the seismo-electric signals (V1) divided by the acoustic pressure difference (V1/ΔP) (Zhu et al. 2013, 2015). The instantaneous ratio of ΔV/ΔP is the experimental value of the streaming potential coefficient of the rock sample (Zhu et al. 2008). In the experimental procedure we improve the signal to noise ratio of the measured seismoelectric signals (V1 and V2) by stacking 1024 measured values .

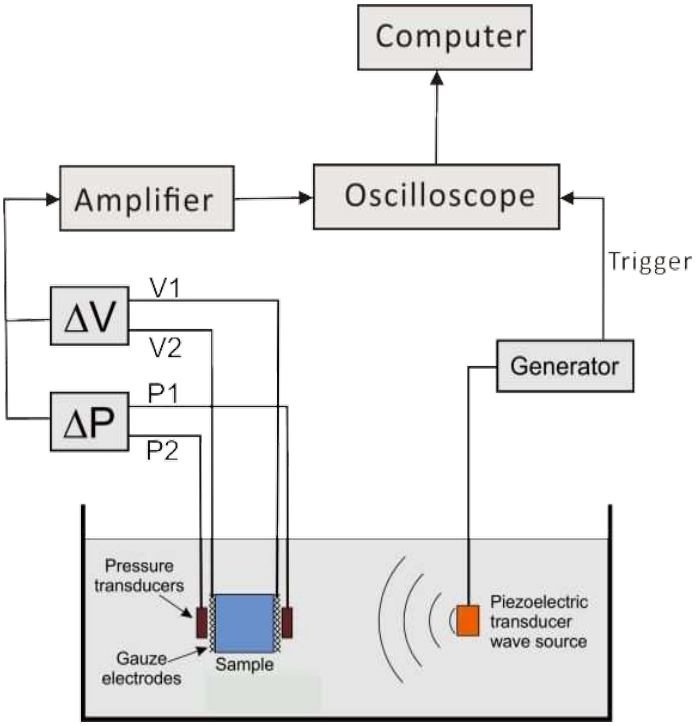

Figure 1. Schematic diagram of the seismo-electric apparatus. The wave source, sample and all transducers and electrodes are placed in a water tank.

In this work we have measured 14 samples of shale from the Sichuan Basin in China. Measurements were made both parallel and perpendicular to the observed bedding plane to provide $L(\omega)$ in the two

directions, as shown diagrammatically in Figure 2. We used X-ray diffraction techniques to obtain the composition of the shale samples. The samples have a characteristic porosity less than 5% (Deng et al. 2015) and permeability of approximately less than 1 mD (Fu 2017). The shales have variable composition with 17%wt. to 29%wt. of various clay minerals together with variable amounts of quartz, K-feldspar and plagioclase feldspar. Full data on this shale samples are available in Table 1.

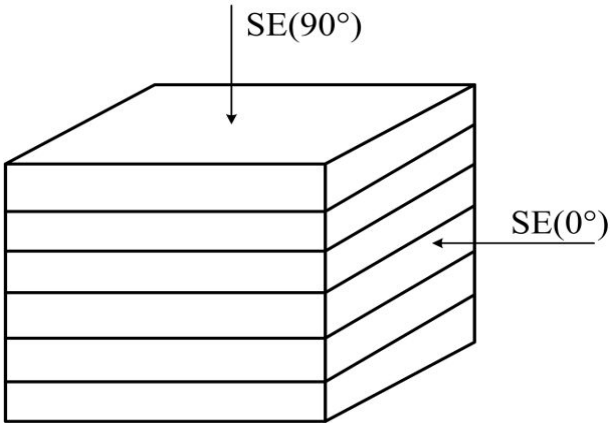

Figure 2. Schematic diagram of shale rock samples. The symbols SE(0°) and SE(90°) represent the seismo-electric measurements parallel and perpendicular to shale bedding, respectively.

We have also measured 5 samples of sandstone from a tight gas reservoir in northwest China. These sandstones have a characteristic porosities and permeabilities in the ranges 1% to 13.7% and 0.235 mD to 58.7 mD, respectively. The sandstones have variable composition with 59.3%wt. to 71.4%wt. of quartz together with variable amounts of feldspar, calcite and muscovite, and less than 5%wt. of clay minerals (wt represents the mass percentage). Full data on the sandstone samples are provided in Table 2.

Table 1. Parameters of the shale samples

Sample	Porosity	0° Permeability (mD)	90° Permeability (mD)	Mean Permeability (mD)	Quartz (%)	K-Feldspar (%)	Plagioclase (%)	Dolomite (%)	Clay (%)	Calcite (%)	TOC (%)
Shale 1	0.0442	0.00074	0.00686	0.00380	61.6	12.4	3.5	-	22.5	-	3.61
Shale 2	0.0247	0.000442	0.00946	0.00495	72.1	7.4	2.6	-	17.9	-	4.01
Shale 3	0.0429	0.000894	0.00205	0.00147	58.9	11.7	4.6	-	24.8	-	3.60
Shale 4	0.0365	0.00300	0.211	0.107	73.7	6.0	1.9	-	18.4	-	4.63
Shale 5	0.0494	0.00120	0.0148	0.00800	57.3	12.3	1.6	-	28.8	-	3.96
Shale 6	0.0145	0.000257	0.00195	0.00110	41.4	7.9	1.9	30.0	18.8	-	3.81
Shale 7	0.0124	0.00130	0.00170	0.00150	36.2	6.4	2.0	36.3	19.1	-	3.04

Shale 8	0.0360	0.000760	0.00264	0.00170	73.3	3.5	3.0	-	20.2	-	3.40
Shale 9	0.0400	0.000491	0.00571	0.00310	67.7	7.4	2.6	-	24.3	-	4.05
Shale 10	0.0410	0.00091	0.00449	0.00270	68.6	6.2	2.4	-	22.8	-	4.00
Shale 11	0.0130	0.00172	0.00256	0.00214	67.7	6.9	2.5	-	22.9	-	3.30
Shale 12	0.0320	0.00151	0.00233	0.00192	48.0	14.8	5.1	4.9	23.2	4	0.88
Shale 13	0.0170	0.00278	0.00506	0.00392	76.1	3.9	2	-	18.0	-	5.02
Shale 14	0.01800	0.00067	0.00253	0.00160	30.1	6.8	1.3	45.0	16.8	-	0.81

Note: Permeability is Klinkenberg-corrected permeability, average permeability of shale means the average permeability tested parallel (0°) and perpendicular (90°) to shale bedding. The porosity is effective porosity acquired by helium porosimetry measurements with the gas volume method. TOC = Total Organic Carbon.

Table 2. Parameters of the sandstone samples

Sandstone samples	Porosity	Permeability (mD)	Quartz (%)	Feldspar (%)	Calcite (%)	Muscovite (%)	Clay (%)
Sandstone 1	0.0621	0.914	64.9	27.4	2.8	2.5	2.4
Sandstone 2	0.124	11.4	71.4	23.6	1.1	1.8	2.1
Sandstone 3	0.137	58.7	64.2	30.2	1.3	1.7	2.6
Sandstone 4	0.0390	10.1	59.3	28.5	4.5	3.5	4.2
Sandstone 5	0.0100	0.235	68.8	26.1	1.8	1.4	1.9

Note: Permeability is Klinkenberg-corrected permeability. The porosity is effective porosity acquired by helium porosimetry measurements with the gas volume method.

All the samples are saturated with NaCl concentration by vacuuming for 8 hours, so that the solution and the fluid in pore space of samples are fully mixed, and then the samples stand for one day to keep the stability of the whole sample and fluid system before measurements.

3.2 Experimental Results

Figure 3 shows a direct comparison of the measured seismoelectric signals for three shale samples and three sandstone samples of varying porosity and permeability together with a reference trace with no seismic source present.

In the absence of a sample (Trace 1) no seismo-electric signal is present but with an interference signal in Trace 1 at the starting moment, this is in accordance with Wang et al. (2020) observed in their experiments. The seismo-electric signals appearing in other 6 traces are those where a sample has been applied, demonstrating that the observed transient electric signals are due to seismo-electric conversion in the rock samples under the excitation of acoustic pressure. This observation is confirmed by calculating the expected arrival time of the seismo-electric signal. In these experiments the source-sample distance was 6±0.1 cm and the pressure wave velocity in the water is about 1500

m/s. Consequently, a seismoelectric signal would be expected to occur 40±0.67 μs after the source pulse. In these experiments the measured electric potential arrived at 39.04±0.5 μs, where the uncertainty reflects the spread of measurements and the experimental uncertainty, and this is the one way travel-time of the pressure wave from the source to the sample.

In Figure 3 the size of the seismo-electric signal increases with the increasing porosity and permeability for sandstones. For example, the seismo-electric coupling is relatively weak for Sandstone 1 (k=0.914 mD), but larger for the sandstone samples which have higher permeabilities. On this basis, one might expect the amplitude of the seismo-electric signals of the much lower permeability shales (0.00147 to 0.00495 mD) to be extremely small and perhaps unmeasureable. However, that is not the case. Figure 3 shows seismo-electric signals for shales of 0.00495 mD permeability (Shale 2; Trace 6) with amplitudes as large as those for samples with permeabilities 4 orders of magnitude larger (58.7 mD; Sandstone 3; Trace 4). In summary, although the magnitude of the seismoelectric signals is related to porosity and permeability for both sandstones and shales, the seismoelectric signals of shales are comparable to those of the sandstones even though the shales have much lower permeabilities.

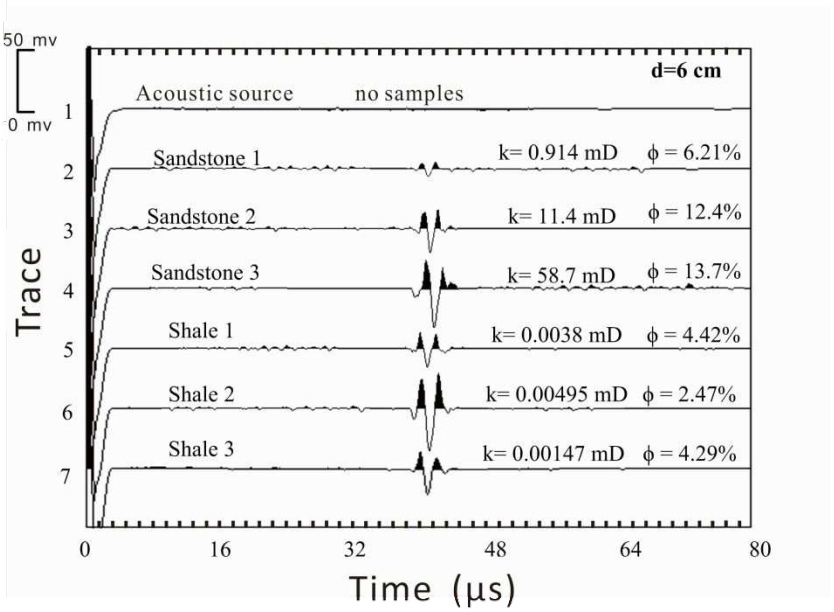

Figure 3. The measured seismoelectric signals (V1) of sandstones and shales at T=25°C, in water and with a source-sample distance of 6 cm. The floating y-axis scale refers to all traces and is relative to the baseline of each trace. The permeability, k, and porosity, ϕ, of each sample is also given.

We hypothesize the existence of some other characteristic that enhances seismo-electric conversion in shales so they can provide comparable seismo-electric signals' amplitudes despite the shales having permeabilities approximately 5 orders of magnitude smaller than the sandstones.

The experimental measurements show that the amplitude of the induced seismo-electric signal is also dependent on anisotropy. Figure 4 shows the seismo-electric signals measured in each of two orthogonal directions on 3 shale samples (Figure 4a) and on 3 sandstones (Figure 4b). In this experiment the distance between the acoustic source and the rock sample was 8±0.1 cm. Taking the acoustic velocity in water to be about 1500 m/s, as before, predicts the seismo-electric conversion signal to arrive at about 53.33±0.67 μs. Experimentally measured value, which can be read from Figure 4 was 52.5±0.5 μs.

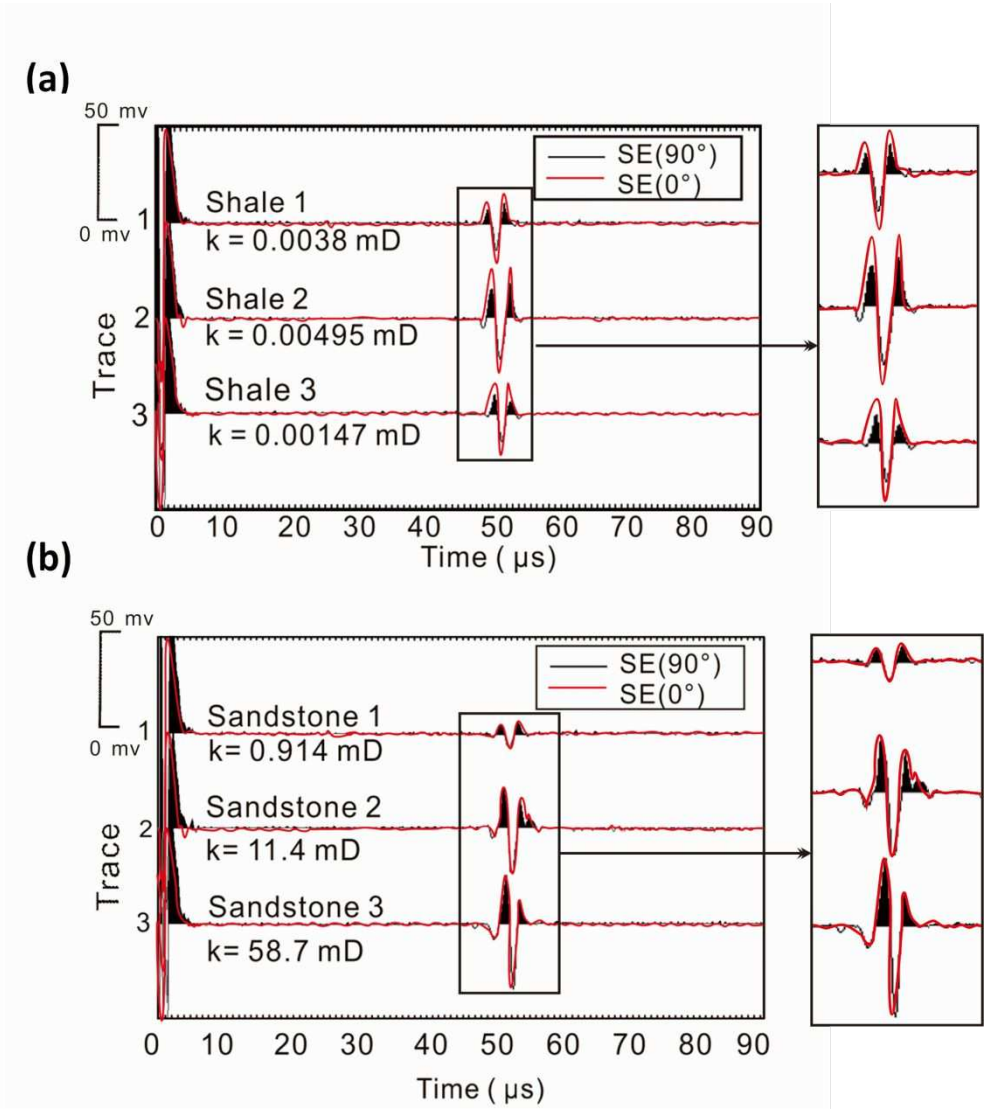

Figure 4. The seismoelectric signals of (a) 3 shale samples, and (b) 3 sandstone samples. The signals measured parallel to the shale bedding (red line) are much larger than those measured perpendicular to the shale bedding (in-filled black line) in the case of the shales, but there is no difference for the sandstones.

In Figure 4a the measurements for shale samples made parallel to bedding (*SE(0°)*, red line) and vertical to the shale bedding (*SE(90°)*, in-filled black line) are different, with the measurements parallel to the shale bedding (red line) being significantly larger than those measured perpendicular

to the shale bedding (in-filled black line). Clearly, the anisotropy of the shale has a measureable effect on the strength of seismo-electric conversion. This contrasts with the situation for sandstones. For sandstones measured in this work (Figure 4b), no bedding was observable. Consequently, the two orthogonal measurements given in the figure, though made perpendicular to each other, are not related to a bedding plane. These two measurements behave in the same way and have the same intensity. Consequently, it might be said that measurements of the amplitude of the seismo-electric signals in the sandstones exhibit isotropic seismo-electric conversion, as would be expected.

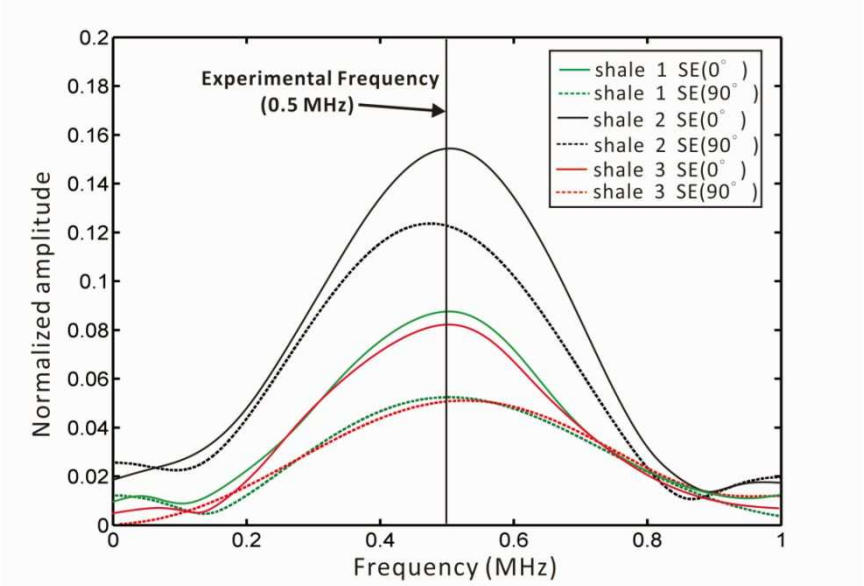

Figure 5. The frequency spectra of seismoelectric signals for the 3 shale samples whose data appear in Figure 4.

Analysis of the frequency spectra of the induced seismoelectric signal has been carried out for all shale samples and for both directions of measurement. Figure 5 shows the seismoelectric signal frequency spectra for those sample traces shown in Figure 4. In all cases the modal frequencies of the spectra correspond approximately to the frequency of transmitting transducer (0.5 MHz). For measurements parallel to the bedding the modal peak falls in the range 0.5±0.008 MHz. By contrast, the frequency spectra of seismoelectric signals made perpendicular to bedding exhibit smaller amplitudes, as also seen in Figure 4, and are broader, with a modal peak value which falls in the broader range 0.5±0.05 MHz. The process which broadens the spectra for measurements made perpendicular to the bedding in shales is not currently known.

Most of the experimental results conform to what might been expected. The most interesting unexplained observation is that seismoelectric coupling, while it clearly depends on porosity and permeability for both shales and sandstones, is equally strong for shales than for sandstones even though shales have a much lower permeability. We have carried out numerical modelling of the Pride (1994) theory of frequency-dependent seismo-electric conversion in porous media in order to

try to understand the effect. Numerical modelling has also been carried out to ascertain whether it is possible to model our experimental measurements on both shales and their corresponding sandstones. An associated objective was to understand the sensitivities of the amplitude and phase of the generated seismoelectric signals to a number of important rock parameters, including porosity, permeability, tortuosity, zeta potential and dimensionless number occurring in Equation (1).

4 Numerical modelling

4.1 Modelling methodology

This section is dedicated to examining how the frequency dependence of the seismo-electric coupling coefficient $L(\omega)$ depends on major rock parameters. In order to do this the Helmholtz-Smoluchowski (Equation (6)) and the Pride (Equation (1)) relationships have been implemented in the frequency domain using numerical modelling with Matlab.

The Helmholtz-Smoluchowski relationship for C_{sp0} (Equation (6)) and the Pride relationship for $L(\omega)$ (Equation (1)) imply that there are many factors affecting the seismo-electric conversion. These include the transition frequency ω_c, the Debye length $\tilde{d}$, the skin depth δ, the characteristic length scale of the pores Λ, the dimensionless number m^*, porosity ϕ, permeability k_0, tortuosity α_∞ and zeta potential ζ.

In this work we assume the Debye length $\tilde{d}$ of shale and sandstone in NaCl solution are the same, equal to 3.0709×10^{-6} m, and can be written as (Debye & Hückel 1923)

$$\tilde{d} = \sqrt{\frac{\varepsilon_f k_B T}{2000 N e^2 I_f}}\ , \tag{7}$$

where ε_f is the absolute permittivity of the fluid, k_B is Boltzmann's constant, T is absolute temperature, N is the Avogadro's number defined as $N=6.022\times10^{23}$ in molarity, e is the electric charge, and I_f is the ionic strength ($I_f = \frac{1}{2}\sum_{i=1}^{n} c_i z_i^2$), where Z_i is the ionic valence ($Z = 1$ for an NaCl solution),and C_i is the molar concentration of the ions in the fluid. For a NaCl solution, $I_f = C$, where C is the fluid concentration. This assumption remains valid providing the temperature and salinity of the pore fluid remains unchanged. We also assume that the skin depth δ ($\delta = \sqrt{\frac{\eta}{\omega\rho_f}}$) for shale and sandstone are also identical (i.e., the same pore fluid with the same density and viscosity is present in both rocks). Hence, we present numerical modelling results for the variation of frequency-dependent eismo-electric coupling coefficient $L(\omega)$ as a function of frequency and m^*, porosity, permeability, tortuosity and zeta potential.

In addition to the variables examined by numerical modelling, there are also some variables which are either fundamentally constant or that we have held constant for the purposes of the modelling. These values are shown in Table 3.

Table 3. Parameters used in numerical modelling of frequency-dependent seismo-electric coupling coefficients.

Parameters	Symbol	Values used in modelling	Unit
Fluid viscosity	η^1	0.001	$N.s/m^2$
Fluid concentration	C	1×10^{-5}	mol/L
Water density	${\rho_f}^1$	1000	kg/m^3
Absolute temperature	T^1	298	K
Ion concentration	N^1	6.022×10^{23}	$ions/m^3$
Charge of an electron	e^1	1.602×10^{-19}	C
Boltzmann's constant	${k_B}^1$	1.381×10^{-23}	J/K
Fluid permittivity	${\varepsilon_f}^1$	$80 \times 8.854 \times 10^{-12}$	F/m
Sample permittivity	${\varepsilon_r}^1$	$4 \times 8.854 \times 10^{-12}$	F/m
Tortuosity	α_∞	[2, 4, 6, 8, 10]	-
Porosity	ϕ	[0.0001, 0.001, 0.05, 0.1, 0.5]	-
Permeability	k_0	[0.001, 0.01, 1, 50, 1000]	mD
The dimensionless number	m^*	[6, 8, 12, 14, 18]	-
the characteristic length scale of the pores	Λ	[0.01, 0.05, 0.1, 0.3, 1]	μm
Zeta potential	ζ	[0.01, 0.1, 1, 10, 100]	mV

[1]Zhu et al. (2015)

4.2 The effect of dimensionless number

The dimensionless number m^* describes the geometric characteristics of pore space and consists only of the pore-space geometry terms (Equation (4)). Figure 6 shows the effect of the dimensionless number m^* on seismo-electric coupling coefficient $L(\omega)$. Values of m^*=8 and m^*=12 are the characteristic for sandstone and shale (Johnson et al. 1987). We chose to model m^*=6, 8, 12, 14, 18 to see the influence of dimensionless number m^* on $L(\omega)$ and including the accepted values of m^* for sandstone and shale. In modelling $L(\omega)$ as a function of frequency and m^*, porosity, permeability, tortuosity and zeta potential were all kept constant, with ϕ=10% (0.1), k_0=10 mD, α_∞=3, and ζ=-40 mV.

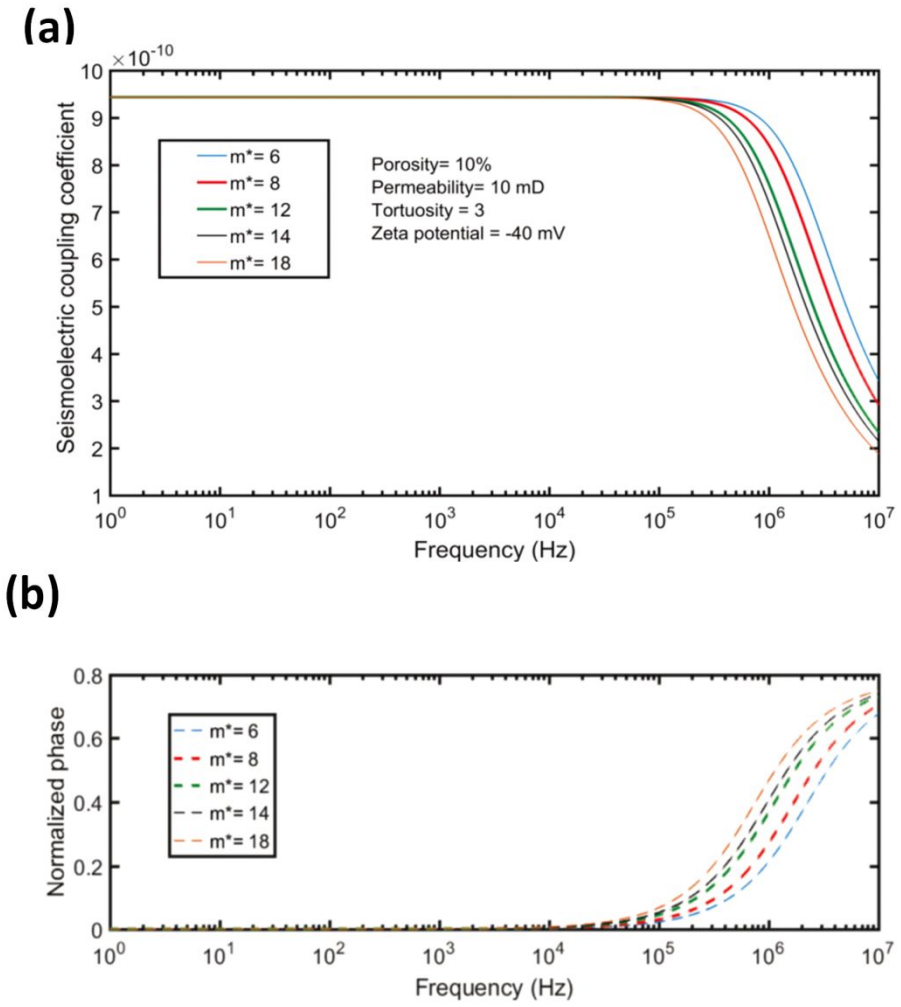

Figure 6. The effect of varying the dimensionless number m^* on modelled frequency-dependent $L(\omega)$, with ϕ=10% (0.1), k_0=10 mD, α_∞=3, and ζ=-40 mV all held constant. The two bold curves m^*=8 and m^*=12 are the reported values for sandstone and shale, respectively (Johnston et al. 1987), the solid line (a) and dashed line (b) are the amplitudes and the phases of the $L(\omega)$, respectively.

Figure 6 clearly shows that the amplitude and phase of the seismo-electric coupling coefficient are independent of m^* when the frequency is lower than 100 kHz. Above this frequency an increase in m^* shifts the dispersion in the $L(\omega)$ to lower frequencies, decreasing the critical frequency. However, the effect is small. For example, at 1000 kHz the difference in amplitude of the seismo-electric coupling coefficient resulting from the change of dimensionless number from m^*=8 to m^*=12 is only about 6×10^{-11}. Hence, the dimensionless number has a little influence on the seismo-electric coupling over a large frequency range (0-1000 kHz). One interpretation of this phenomenon is that the seismo-electric coupling coefficient is not affected by large scale microstructure and disorder in a

porous medium (Charlaix et al. 1988). However, it is possible that other mechanisms might give rise to frequency-dependence at low frequencies such as Stern plane polarization.

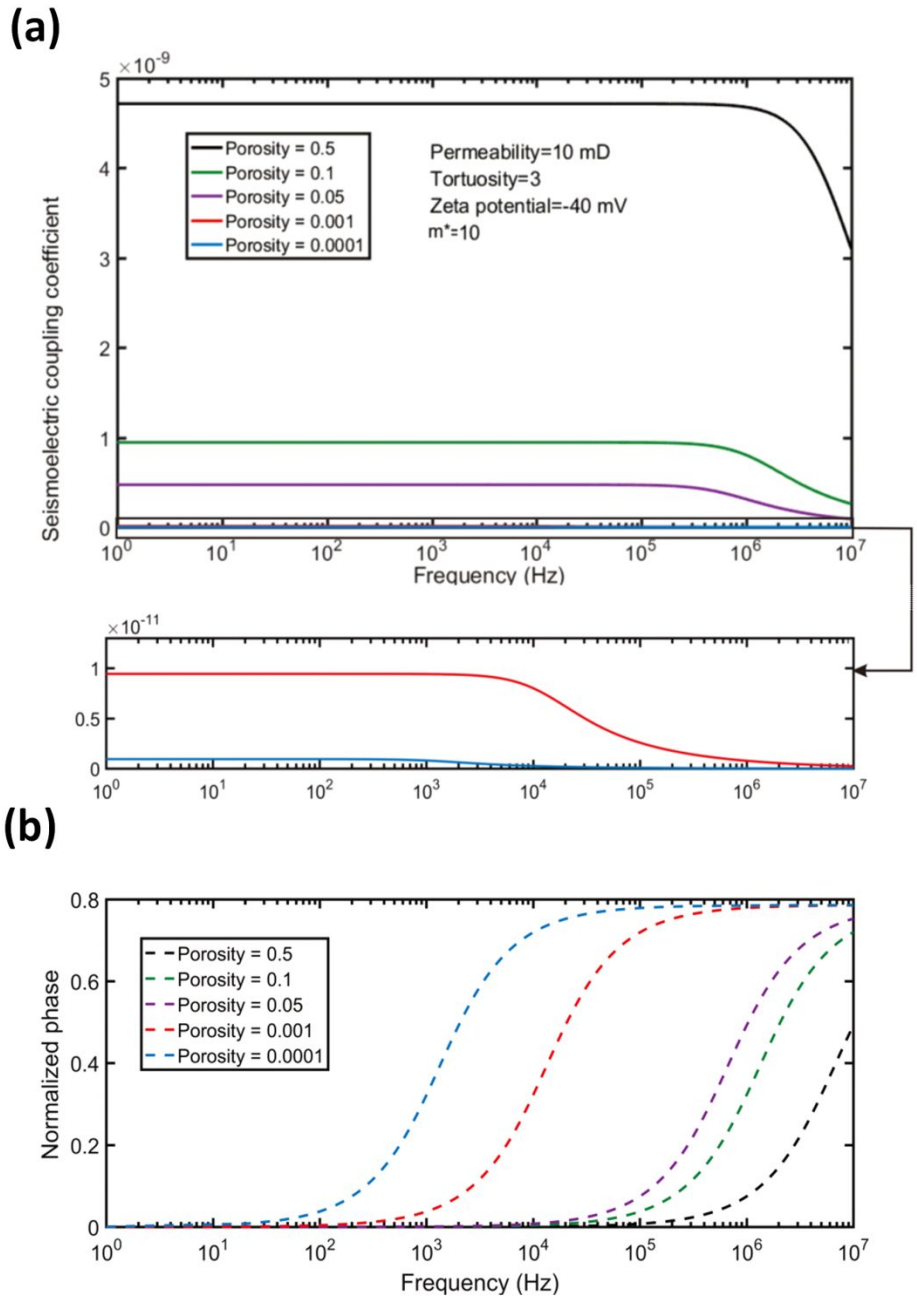

Figure 7. The effect of changing porosity on (a) the amplitude, and (b) the phase of the frequency-dependent $L(\omega)$ as a function of frequency. Other parameters, m^*=10, k_0=10 mD, α_∞=3, and ζ=-40 mV held constant.

4.3 The effect of porosity

When modelling the effects of porosity we have to cover a wide range of values. The porosity of conventional sandstones is generally in the range 5% to 30% (0.05 to 0.30). By comparison shales may have an even wider range of porosities, from Sichuan shales which have values less than 5% (Deng et al. 2015) to some gas shales with porosities approaching 30% (0.30). Consequently, we have carried out modelling from 0.01% to 50% (0.0001 to 0.5) in order to capture all possible values. During the modelling $L(\omega)$ as a function of frequency and porosity, the dimensionless number, permeability, tortuosity and zeta potential were all kept constant, with m^*=10, k_0=10 mD, α_∞=3, and ζ=-40 mV.

Figure 7 shows how varying the porosity of the porous medium affects the amplitude and phase of the frequency-dependent seismo-electric coupling coefficient. The range of modelled values is so great that the results for the smaller porosities are shown on an expanded scale in the inset of the figure. It is clear that values of the amplitude of the $L(\omega)$ are very small ($<5\times10^{-11}$) for porous media whose porosity is less than 5% (purple line). As porosity increases there is an increase in the amplitude of the $L(\omega)$ by about 3.5 orders of magnitude (from about 1×10^{-12} to just under 5×10^{-9}) as well as an increase in the critical frequency from about 1 kHz for ϕ=0.0001 (0.01%) to about 10 MHz for ϕ=0.5 (50%). Hence, the numerical modelling results indicate that porosity has a strong effect on the amplitude of low frequency seismo-electric coupling as well as the frequency at which dispersion occurs.

4.4 The effect of the characteristic length scale of the pores (Λ)

Figure 8 is the image analysis of scanning electron microscopy from the shale samples in the southern Sichuan Basin (Wang et al. 2014). The shale in Longmaxi formation in Sichuan Basin is mainly composed of intergranular pores, inter-crystalline pores, organic matter pores and fossil interpores. The first four pore types belong to inorganic type, while the latter two pore types are organic type.

The pore size in the shale samples from Sichuan Basin is mainly from nanometer to micrometer scale. The matrix pore size is generally less than 2 μm, and its main pore length is in the range of 0.1-1 μm. The pore size of organic matter is mostly from 0.01 μm to 0.3 μm. The pore morphology is mainly round, elliptical and irregular and the pore characteristics of Sichuan shale are similar to the Barnett shale in North America (Wang et al. 2014; Zhang et al. 2014; Liu et al. 2019).

Consequently, we have carried out modelling for characteristic length scale of the pores (Λ) covering the entire range of observed length scales, viz. 0.01 μm, 0.05 μm, 0.1 μm, 0.3 μm, 1 μm, in order to examine the effect of altering the length scale of pores on the seismo-electric coupling. Figure 9 shows the effect of the characteristic length scale of the pores in numerical results. The red curve

corresponds to the smallest pore size (0.01μm), and shows the smallest seismo-electric coupling coefficients. The low frequency seismo-electric coupling coefficient increases as pore length scale increases, seeming to reach a limiting behaviour. Increasing the value of pore length reduces the value of the critical frequency, producing dispersive behavior at lower frequencies as the pore scale increases. This corresponds with structures at larger pore scales causing lower frequency (longer period) dispersion, from which we infer a dispersive process with a fixed mobility or transport rate.

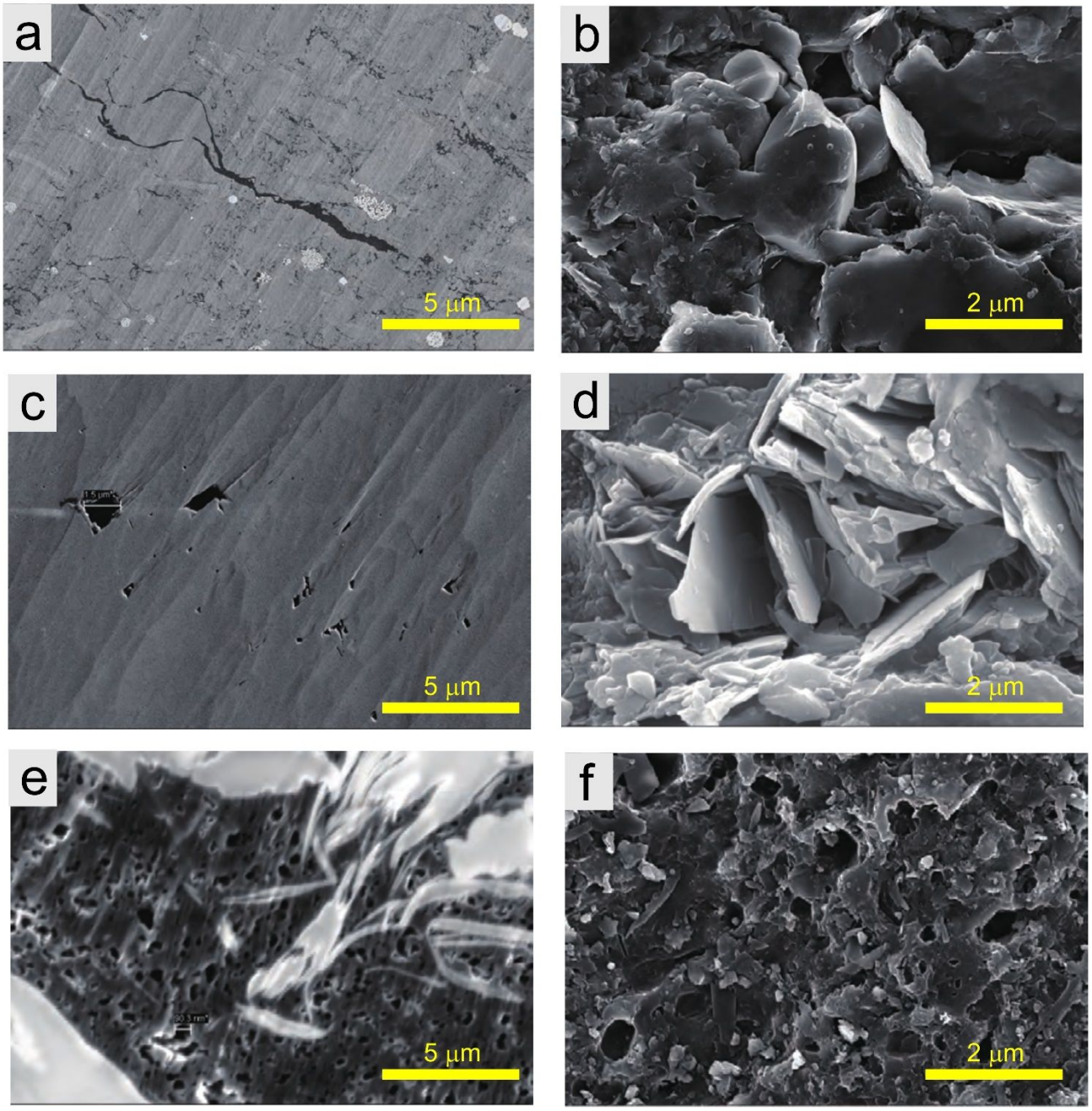

Figure 8. Image analysis of scanning electron microscopy from the shale samples in the southern Sichuan Basin. (a) Microfractures filled with organic matter, (b) inter-granular pores of quartz, (c) inter-granular pore

after argon ion polishing, (d) inter-crystalline pores, (e) pores of organic matter, (f) internal pores of graptolite (Wang et al., 2014).

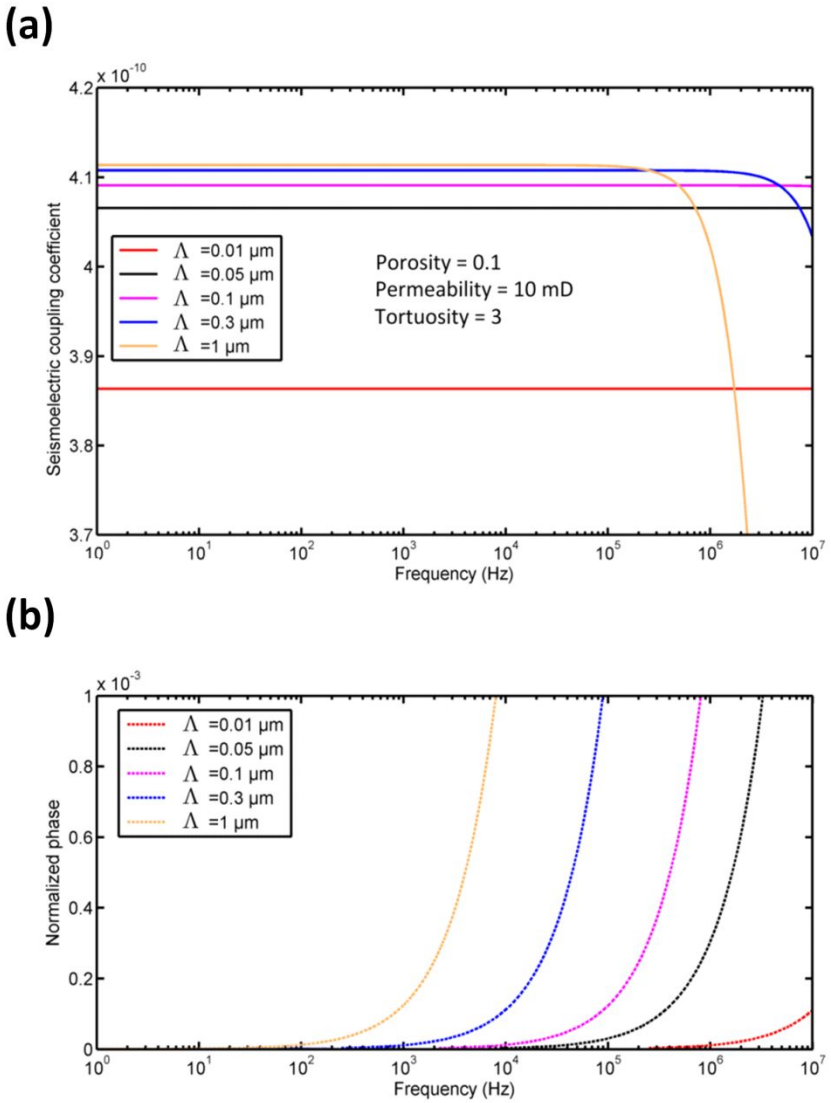

Figure 9. The effect of changing pore length on (a) the amplitude, and (b) the phase of the frequency-dependent $L(\omega)$. Other parameters, ϕ=10% (0.1), α_∞=3, and κ=10 mD held constant.

4.5 The effect of permeability

Numerical modelling has also shown that the frequency-dependent seismo-electric coupling coefficient depends upon permeability in a complex way. Modelling has been carried out for five values of permeability as a function of frequency. The modelled numerical values of permeability are 100 nD, 10 μD, 1 mD, 50 mD and 1 D, while keeping the dimensionless number, porosity, tortuosity and zeta potential constant at m^*=10, ϕ=10% (0.1), α_∞=3, and ζ=-40 mV. This range of

permeabilities covers most sandstones and shales, with most conventional reservoir sandstones falling in the range 50 mD<k_0<1 D, tight sandstones and carbonates falling in the range 50 μD<k_0<50 mD, and most shales having k_0<10 μD and usually in the hundreds of nanodarcies. The permeability of Sichuan shale is less than 1 mD (Fu 2017).

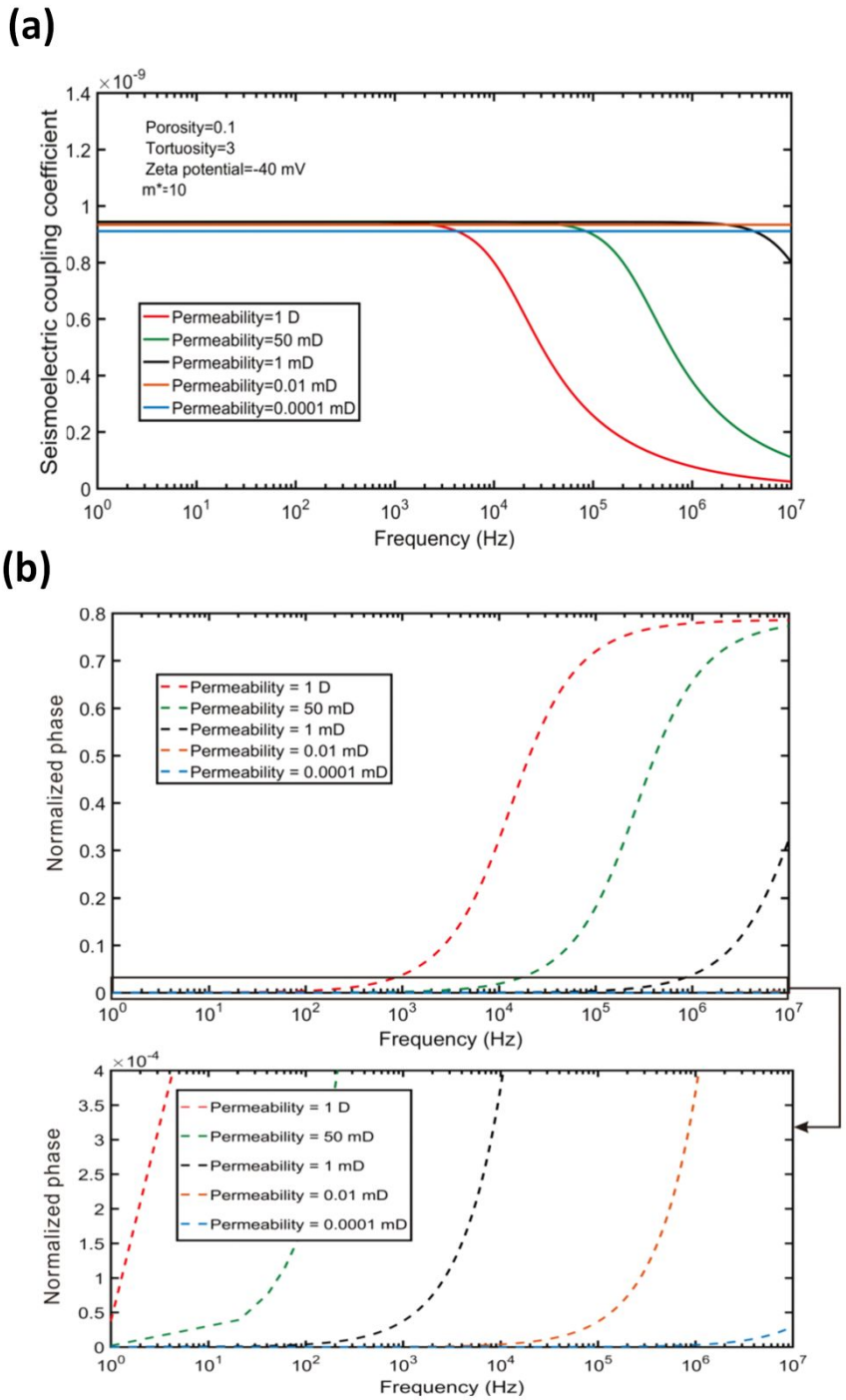

Figure 10. The effect of changing permeability on (a) the amplitude, and (b) the phase of the frequency-dependent $L(\omega)$. Other parameters, m^*=10, ϕ=10% (0.1), α_∞=3, and ζ=-40 mV held constant.

The numerical modelling results displayed as Figure 10 show that, for the sandstone permeabilities (k_0=1 D, 50 mD; red line, green line, respectively), the amplitude of the seismo-electric coupling coefficient is independent of frequency at frequencies below about 1 kHz, which is also indicated by the phase of the seismo-electric coupling coefficient being close to zero for these frequencies. The amplitude of this low frequency behaviour depends very little on permeability, sharing the same value. Dispersion occurs at higher frequencies with the critical frequency occurring at about 10 kHz for k_0= 1 D and increasing to about 200 kHz for k_0=50 mD. The same pattern continues into the tight clastic rock range of permeabilities (k_0=1 mD, 10 μD; black line, brown line, respectively) and then for the shale permeability range (k_0=100 nD; blue line), with the range of frequency independent behavior increasing, the value of the critical frequency increasing and surpassing 10 MHz, and seeing a small decrease in the amplitude of the seismo-electric coupling coefficient for the lowest permeabilities.

This behavior is important as it implies that the strength of seismo-electric coupling in shales is not affected by their low permeabilities, sharing approximately the same value of seismo-electric coupling coefficient as rocks with permeabilities 7 orders of magnitude larger (providing they share the same values of dimensionless number, porosity, tortuosity and zeta potential). Such behavior accords well with our experimental results, and confirms that the similar measured seismo-electric coupling coefficient for shales and sandstones is relatively independent of their very different permeabilities, but rather controlled by their porosities which are different, but not to the same degree that the permeabilities vary.

4.6 The effect of tortuosity

Tortuosity also affects both the amplitude and the phase of the seismo-electric coupling coefficient, as shown in Figure 11. We have carried out numerical modelling of the amplitude and phase of the seismo-electric coupling coefficient for 5 values of tortuosity (α_∞=2, 4, 6, 8, 10) while keeping the other parameters constant (m*=10, ϕ=10% (0.1), k_0=10 mD, and ζ=-40 mV). This range of tortuositys is equivalent to a range of cementation exponents of m=1.2 to 2 for a porous medium of 10% porosity, according to the relationship $\alpha_\infty=\phi^{1-m}$ (Glover 2012).

The amplitude of the seismo-electric coupling coefficient is independent of frequency at low frequencies and undergoes dispersion at higher frequencies. The value of the low frequency (steady-state) seismo-electric coupling coefficient is very sensitive to changes in tortuosity, decreasing from about 1.4×10-9 to 0.3×10-9 as the tortuosity increases from 2 to 10. The onset of dispersive behaviour is also sensitive to tortuosity, but less so than the steady-state seismo-electric coupling coefficient. If we take critical frequency as a measure of the frequency at which dispersion

occurs, the critical frequency decreases from about 2 MHz to about 300 kHz as tortuosity increases from 2 to 10.

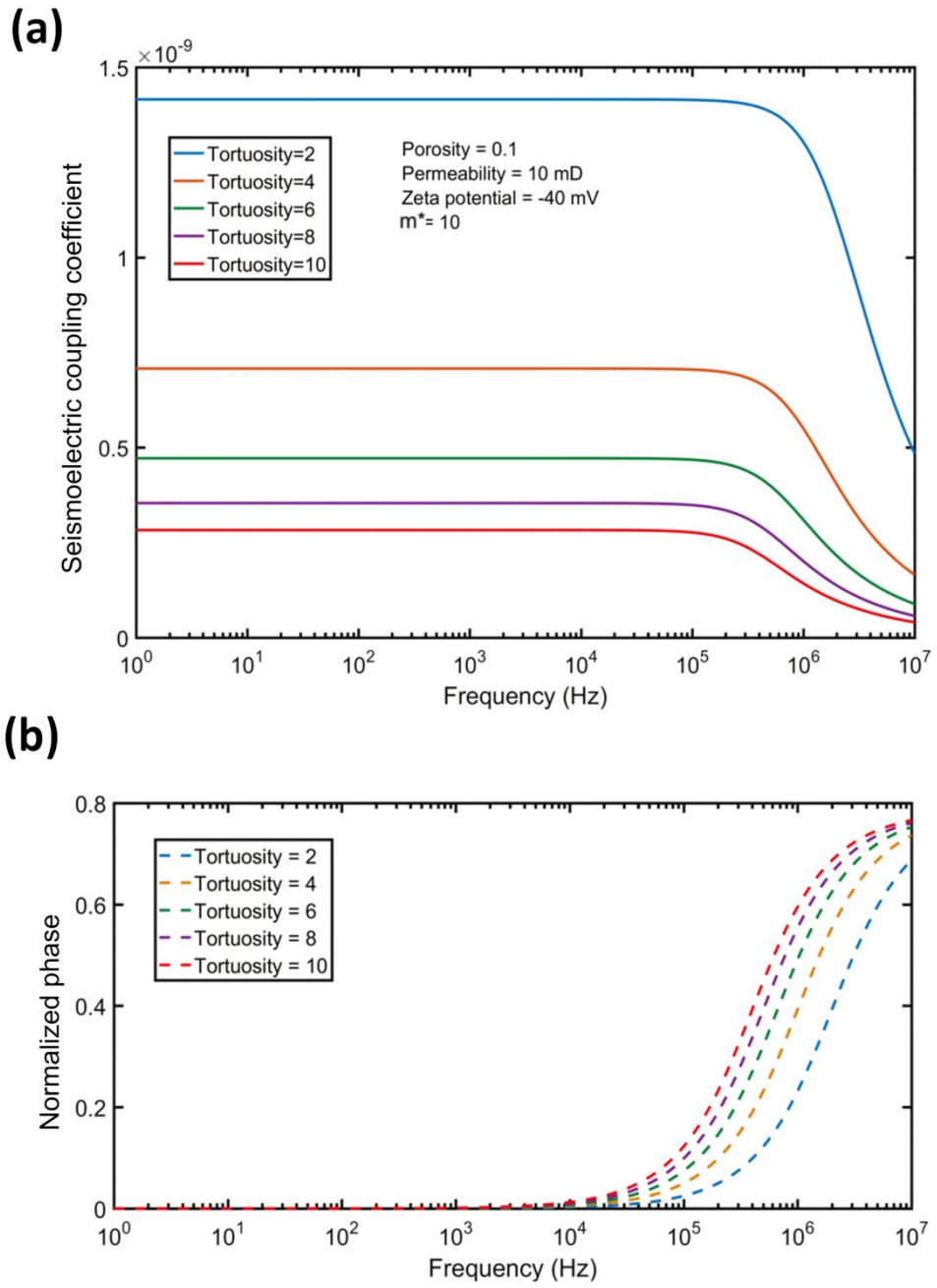

Figure 11. The effect of changing tortuosity on (a) the amplitude, and (b) the phase of the frequency-dependent $L(\omega)$. Other parameters, m^*=10, ϕ=10% (0.1), κ=10 mD, and ζ=-40 mV held constant.

The variation of $L(\omega)$ with tortuosity has implications for measurements made on shales. Shales generally have higher values of tortuosity, which would be expected to lead to a lower strength of seismo-electric coupling, and for a smaller frequency range. However, given that the critical frequency for a tortuosity of 10 is as high as 300 kHz, this restriction is very unlikely to be important as it is much higher than seismic frequencies.

4.7 The effect of zeta potential

Zeta potential strongly affects the amplitude of the seismo-electric coupling coefficient but has no effect on its phase, as shown in Figure 12. Numerical modelling of the amplitude and phase of the seismo-electric coupling coefficient has been carried out for 5 values of zeta potential from -0.01 mV to -100 mV in order of magnitude steps, while keeping all other parameters constant (m^*=10, ϕ=10% (0.1), κ=10 mD, and α_∞=3). This range of zeta potentials covers almost the entire range of values measured experimentally (Walker & Glover 2018), where the maximum zeta potential value is about -150 mV and the minimum is about -2 mV.

Once again the amplitude of the seismo-electric coupling coefficient is independent of frequency at low frequencies and undergoes dispersion at higher frequencies. The value of the low frequency (steady-state) seismo-electric coupling coefficient is approximately linearly sensitive to changes in tortuosity, increasing over 4 orders of magnitude from about 2×10-13 to almost 2.5×10-9 as the zeta potential also increases by four orders of magnitude, from -0.01 mV to -100 mV.

Unlike the other variables examined in our modelling, varying the zeta potential has no effect on the critical frequency. This is expected since the zeta potential does not occur in the frequency-dependent terms in Equation (1).

The numerical modelling confirms the expectation that the zeta potential is critical to the control of the steady-state seismo-electric coupling coefficient, defining its low frequency behaviour, but has no role in controlling the frequencies at which dispersion occurs as characterised by the critical frequency.

4.8 Low frequency behaviour

The seismoelectric coupling coefficient is a function of frequency but only at high frequencies. The value of the constant, low frequency behavior depends strongly on porosity, tortuosity and zeta potential, but very little on permeability, and is independent of the dimensionless number. This behaviour is consistent with Equation (6), which describes the low frequency behavior of the $L(\omega)$. However, Figure 8 shows that there is a slight dependence of $L(\omega)$ on permeability for very low permeabilities. This may be due to the assumption $\tilde{\boldsymbol{d}} \ll \Lambda$ breaking down as Λ becomes very small in low permeability shales. Consequently, we may expect that the low permeability may also reduce the strength of seismo-electric coupling in shales.

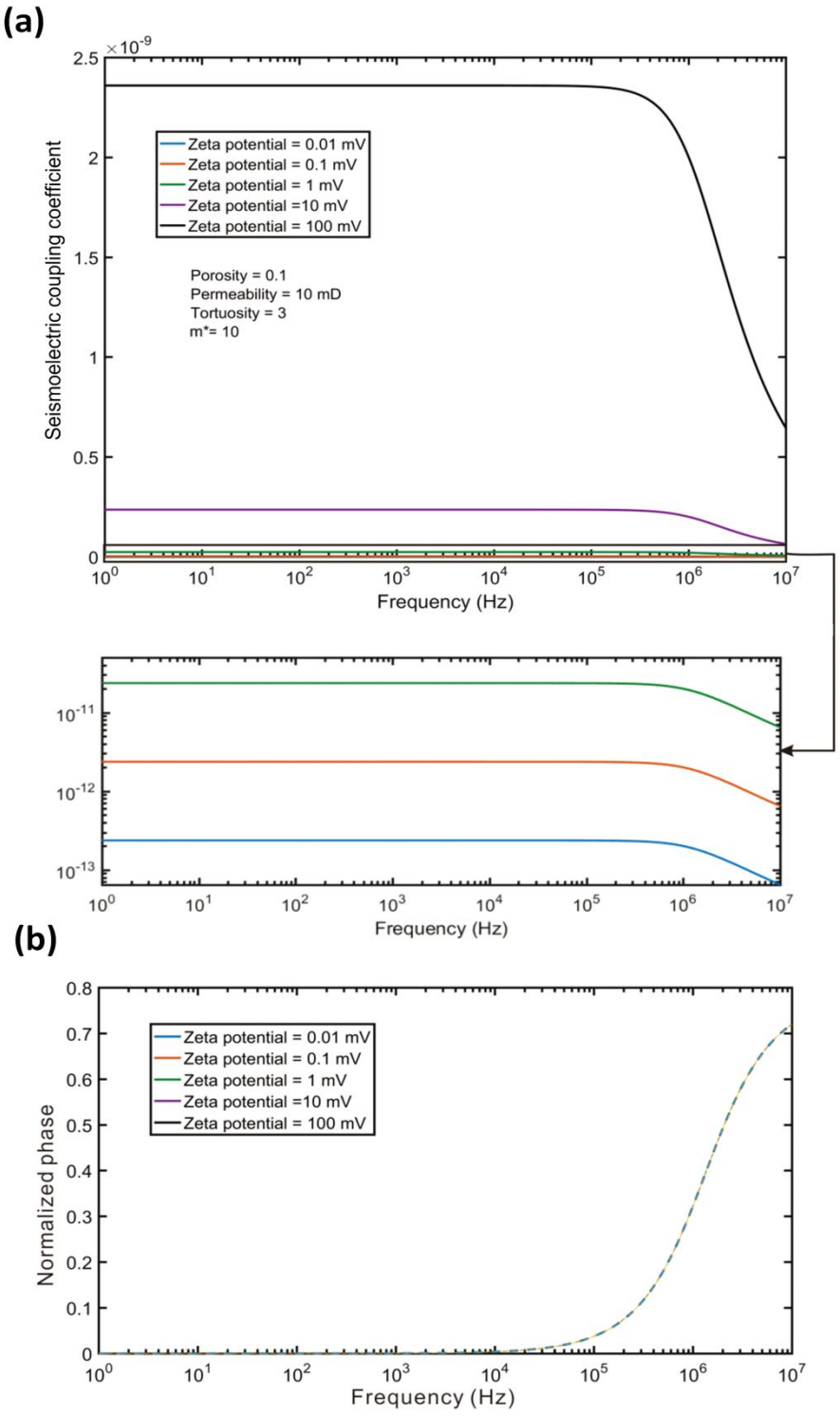

Figure 12. The effect of changing zeta potential on (a) the amplitude, and (b) the phase of the frequency-dependent $L(\omega)$. Other parameters, m^*=10, ϕ=10% (0.1), κ=10 mD, and α_∞=3 held constant.

Examination of the variables controlling the seismo-electric coupling coefficient $L(\omega)$ in this section, leads us to recognize that for most relevant frequencies, porosity, tortuosity and zeta potential are most important. However, the porosity of the Sichuan shales is low in this work, and their tortuosity is high (Chen et al. 2015). Both of these observations conspire to reduce the strength of seismo-electric coupling. That seismo-electric coupling is at least as great as that found in sandstones is observed experimentally implies, therefore, that the shales must exhibit a higher zeta potential. Furthermore, such an enhanced zeta potential should be related to the mineralogical composition of the rock. This hypothesis is explored in the last section of this paper.

Typical shale values (say, m^*=12, ϕ=5% (0.05), k_0=0.005 mD, α_∞=2.66 (α_∞= (1-2.02ln0.05)$^{1/2}$ = 2.66, and ζ=-100 mV) lead to a low-frequency seismo-electric coupling coefficient of approximately 1.344×10^{-9} at 100 Hz. This value represents a strong seismo-electric effect which can explain the experimental observations (Figure 3) described earlier in this paper. We have carried out further numerical modelling matched to the experimental conditions in order that the modelling results can be compared directly with the experimental measurements. This work is described in the next section.

4.9 High frequency behaviour

At higher frequencies dispersion occurs, reducing the amplitude of the $L(\omega)$ and increasing its phase ultimately to $\pi/2$ radians. The frequency at which this behavior occurs is characterized by a critical frequency, which is defined as the frequency where the phase angle is $\pi/4$ radians. Figures 6 to 10 show clearly that all of the variables tested in this work except the zeta potential affect the critical frequency, sometimes by several orders of magnitude. This is consistent with Equation (1) which contains all of the variables except the zeta potential in the frequency-dependent part of the equation. However, and remembering that we were careful to ensure that our input variables covered the whole range expected for conventional and unconventional reservoir rocks, the critical frequencies are so high that they occur several orders of magnitude above those frequencies encountered in practical exploration seismology. The frequency range of seismo-electric exploration is determined by the seismic and acoustic source. The source frequency of seismic exploration is mainly less than 1000 Hz, and the emission frequency of acoustic source used in well logging is mainly in the range of 2~20 kHz. The seismic source and well logging acoustic source are both used as the source in seismo-electric exploration, hence, the frequency range for the seismo-electric exploration will not exceed 20 kHz. Consequently, it is unnecessary to use frequency-dependent $L(\omega)$ when dealing with seismo-electric applications except when the characteristic frequency exceeds at least 20 kHz.

5. Comparing numerical results with experimental data

We have compared the frequency-dependent amplitude of the seismoelectric coupling coefficient $L(\omega)$ of sandstone and shale samples obtained experimentally earlier in this paper with results from

numerical modelling of the Pride (1994) model but constrained by independently obtained sample characteristics such as porosity, permeability, tortuosity etc. The porosities and permeabilities were measured in the laboratory. The calculation parameters are shown in Table 4.

The zeta potential of solid porous materials is difficult to measure experimentally. It requires the measurement of the seismoelectric coupling coefficient, and then calculation of the zeta potential assuming that the Helmholtz-Smoluchowski equation is valid (Walker et al. 2014). Consequently, in many applications empirical relationships between the zeta potential and the pore fluid salinity are used.

Pride and Morgan (1991) first produced an empirical fit of zeta potential ζ to pore fluid salinity C using 35 data points. They obtained the relationship of the form

$$\zeta = a + b log_{10}(C), \quad \textbf{(8)}$$

with a = -8 mV and b=26 mV, which was later found to arise from a theoretical model for ζ (Revil & Glover 1997; 1998; Revil et al. 1999a) if a number of simplifying assumptions applied. These were (i) that the pH of pore fluid was approximately 7, (ii) that the pore fluid is a Na+ or K+ symmetric electrolyte, (iii) that the influence of H+ and OH− ions on the ionic strength of the solution saturating the pores could be neglected (Revil & Glover 1997), and (iv) that direct adsorption of K+ and Na+ ions upon the silica surface could also be neglected. Consequently, it was implied that the rock would be a sandstone. Recently a fit has been implemented on a very large dataset of sandstones (1253 measurements) (Walker & Glover 2018), which confirms Equation (8) and provides a = -3.505 ± 28.823 mV and b=11.33 ± 4.06 mV. The uncertainty of a and b is because the values obtained are for an aggregation of different samples and rock types at uncontrolled pH.

However, good relationships of the form of Equation (8) for silica-based rocks, and despite the fact that Equation (8) can be derived from EDL equations for silica-based rocks, it cannot be assumed that an equation of this form will be valid for shales, where the presence of stern-plane polarization in clays is an important additional factor. Figure 13 shows 13 measurements of the zeta potential in shales saturated with NaCl and KCl solutions from four sources together with a best fit of Equation (8). The combined datasets shows a considerable scatter, and it is not possible to say that Equation (8) is indicated by the data. If Equation (8) is fitted to the shale data, we obtain a=19.14± 24.32 mV, b=21.07 ± 8.17 mV, with the coefficient of determination R^2=0.874, and is shown by the red line in Figure 13. Many more measurements on shale are required before we can even say that Equation (8) is a valid empirical approximation let alone define its parameters.

Figure 14 shows the numerical and experimental amplitude of the seismoelectric coupling coefficient $L(\omega)$ of sandstones and shale samples as a function of frequency. The experimental data includes an assessment of uncertainty for each measurement based on the propagation of experimental

uncertainties associated with the measurement of the transient seismoelectric potential and transient pressure differences. In each case the experimental measurements agree fairly well with the numerical modelling, indicating that, while not ideal, a model based on the Pride (1994) approach captures the features of the experimental data well.

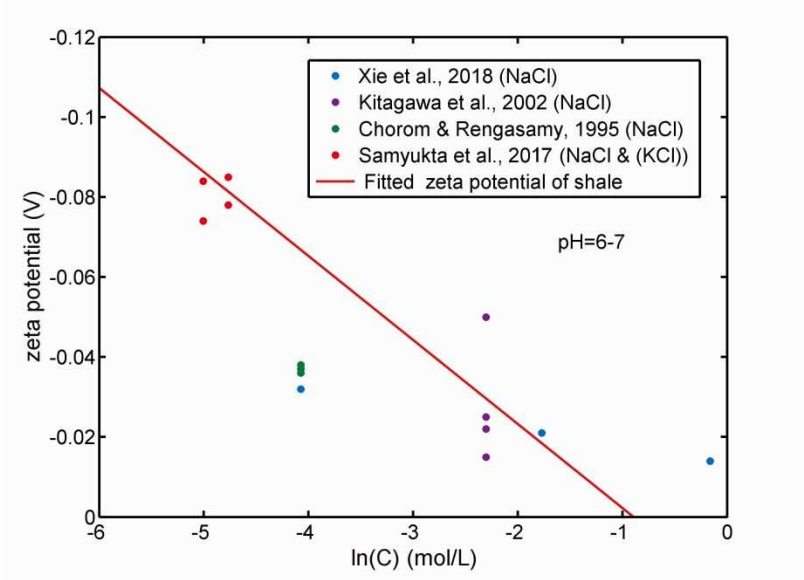

Figure 13. Zeta potential of shales (orange line). The symbols are experimental values of zeta potential measured on shale and clay minerals extracted from previous research for which pH= 6-7.

The fits shown in Figure 14 show that the amplitude of the seismoelectric coupling coefficient for shales is of comparable size and sometimes surpasses that of the sandstones despite the low porosities and permeabilities exhibited by the shales. This phenomenon depends upon the shales having larger zeta potentials. Indeed, the modelling shown in Figure 14 uses an imposed zeta potential function for shales that results in greater zeta potentials than the zeta potential function imposed for the sandstones (see Table 4) for all values of fluid concentration less than 0.02482 mol/dm^3. At the fluid concentration used for the experiments and the modelling (10^{-5} mol/dm^3) the zeta potential for the shale modelling is 1.622 times larger than that used for the sandstone modelling.

6. Seismo-electric coupling and clay mineralogy

Since the experimental and modelling results given in this paper strongly suggest that shales exhibit a larger zeta potential, we have examined their mineralogical composition. Analysis of the mineralogical composition of the 14 samples of Sichuan Basin shale used in this work was carried out by X-ray diffraction (XRD).

Table 4. The input parameters used in numerical modelling of frequency-dependent seismoelectric coupling coefficients of shales and sandstones

Parameters	Symbol	Values of shale used in modelling	Values of sandstone used in modelling	Unit
Fluid concentration	C	1×10^{-5}		mol/dm^3
Tortuosity	α_∞	$\alpha_\infty = \sqrt{1 - 2.02ln(\phi)}$		-
Sample Porosity	ϕ	0.0442, 0.0247, 0.0429, 0.0494, 0.0365	0.137, 0.124, 0.0621, 0.0390, 0.0100	-
Sample Permeability	k_0	0.00380, 0.00495, 0.00147, 0.008, 0.107	58.7, 11.4, 0.914, 10.1, 0.235	mD
Dimensionless number	$m*$	12	8	-
Zeta potential	ζ	$\zeta = 19.14 + 21.07log_{10}(C)$	$\zeta = 3.505 + 11.33log_{10}(C)$	mV

Note. The value for C, ϕ, and k_0 were measured in the laboratory. The value of k_0 was Klinkenberg-corrected and obtained using an ultra-low-permeability measuring instrument (PDP-200). The values for other parameters are from Zhu et al. (2015) and shown in Table 3.

The main minerals composing the shales measured in this report were quartz, plagioclase, K-feldspar and a range of clay minerals, including kaolinite, illite and smectite. Figure 15 shows the relationship between the contents of non-clay and clay minerals, total organic carbon (TOC) and the seismo-electric signals obtained parallel and perpendicular to bedding. The non-clay components of the Sichuan shales are predominantly quartz with smaller amounts of K-feldspar and plagioclase feldspar. Figure 15a indicates that there is no clear relationship between the seismo-electric conversion and the weight fraction of any of the minerals indicating that their presence has no influence over the zeta potential of the rock or the resulting seismo-electric coefficient.

The seismo-electric coefficient is, however, sensitive to the clay composition. Figure 15b shows that the amplitude of the seismo-electric signal increases approximately 60% (from 16±4 mV to 27±4 mV) when the clay mineral fraction increases from 16.8%vol. to 28.8%vol. This indicates that seismo-electric coupling is strongly influenced by the clay content, increasing with the increases in the clay mineral fraction, and implying that the zeta potential also increases significantly as clay content increases.

Zeta potential is directly related to the amount and distribution of the charges at the solid-liquid interface, and characterizes the electric double layer. Shale has the mechanism of generating surface charge (Müller 1996; Fosu-Duah et al. 2016). The surface potential of clay minerals is large compared to that of other reservoir rock-forming minerals such as quartz, calcite and dolomite. So a higher clay mineral fraction will lead to higher surface potentials, thus producing a higher zeta potential (Leroy & Revil 2009; Fosu-Duah et al. 2017). Consequently, the close relationship between increasing clay content and increasing seismo-electric conversion indicates that clay mineral-fluid interactions are the main cause of high zeta potentials and leads to strong seismo-electric conversions in clay-rich shales.

Figure 16 shows the effects of the main components of the clay minerals on seismo-electric (SE) conversion. In our samples the content of kaolinite in the clay is low (0-4%) and there is no evidence for the seismo-electric coupling coefficient depending on the amount of kaolinite in the sample (Figure 16a). There is a substantially greater contribution of mixed illite/smectite, up to about 60%, but here too there is no convincing evidence that this clay structure affects the seismo-electric coupling (Figure 16c). Illite is present in the samples in amounts ranging from 25% to 69%, and as the illite content increases within this range seismo-electric conversion increases by approximately 75% from 16 mV to 28 mV (Figure 16b). This strong functional dependence seems to show that the presence of illite is the main control on the zeta potential in shales.

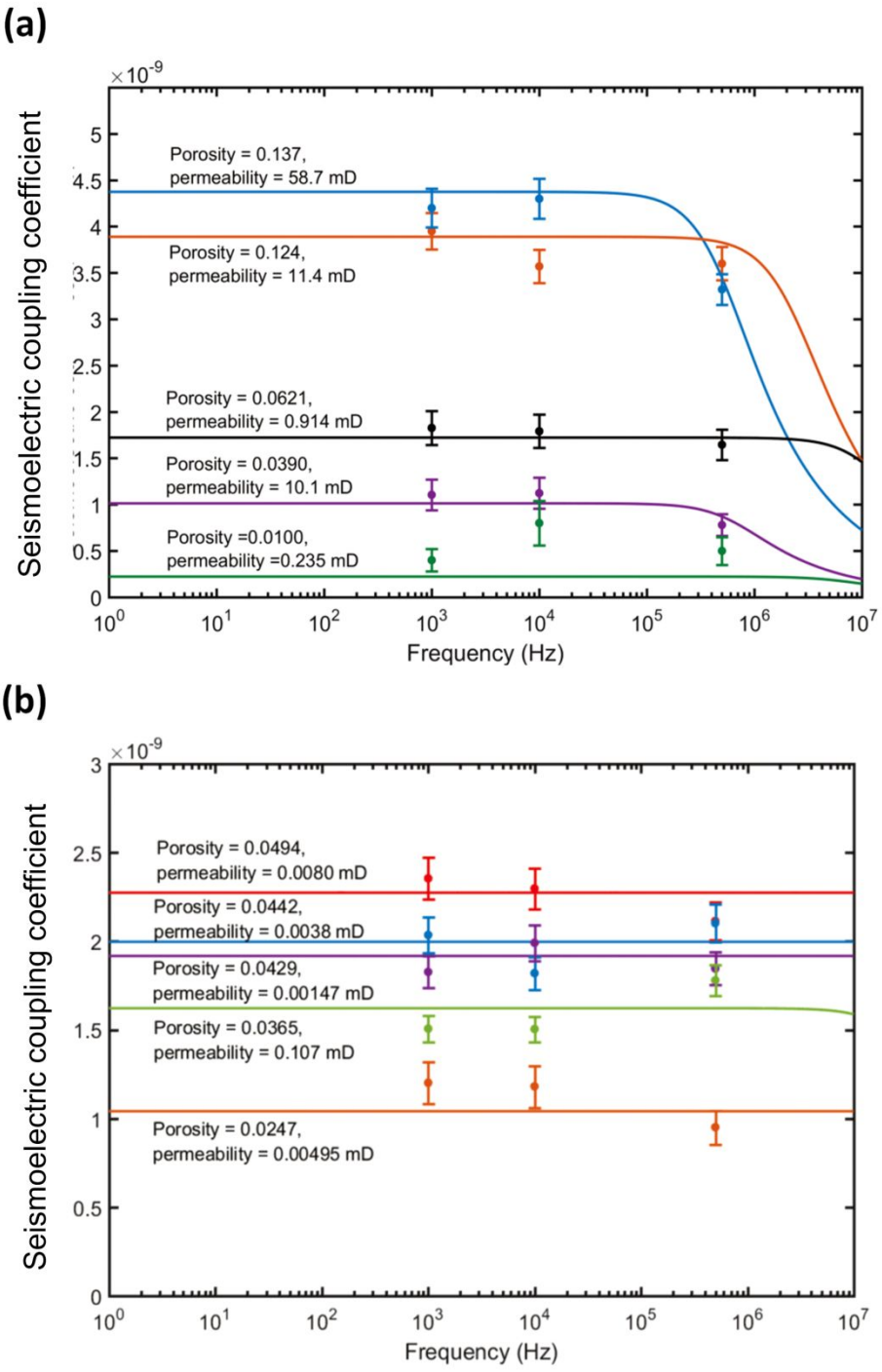

Figure 14. Seismo-electric coupling coefficient as a function of frequency for (a) sandstones, and (b) shale samples. The symbols are the experimental values of $L(\omega)$ which are obtained by taking the arithmetic mean of $L(\omega)$ values obtained parallel and vertical to the shale bedding measured at 1 kHz, 10 kHz and 500 kHz. The error bars represent an uncertainty of about ± 5%. The curves represent modelled seismo-electric coupling coefficient using the Pride theory represented by Equation (1).

We hypothesise that the difference in the efficacy of different clay minerals with regard to seismo-electric coupling is due to differences in their specific surface areas. Kaolinite has a low specific surface area (4 – 16 m^2/g (Bhattacharyya & Gupta 2009)) and hence provides low zeta potentials that cause only small seismo-electric coupling, while Illite has a much higher specific surface area (about 83 m^2/g according to Macht et al. (2011)). There was no Montmorillonite in our samples, but the specific surface area of this clay (346 m^2/g according to Macht et al. (2011)) that it is likely that it would have an extremely large zeta potential and consequent seismo-electric coupling coefficient.

7. Seismo-electric coupling and TOC

The organic carbon component of rocks is expressed by the total organic carbon (TOC) measurement. The value of TOC is expected to be negligible or low in sandstones, but raised in shales because the organic component of some shales provide a source of hydrocarbons and some are exploitable as shale oil and shale gas resources. The lower limit of TOC for gas shales in the USA is considered to be between 2% and 3% (Rezaee & Rothwell 2015; Lu et al. 2012), while some US plays have TOC values extending to 10% (Rezaee & Rothwell 2015). Since the presence of organic carbon is likely to interfere with water-wet flow pathways, we hypothesise that it is possible, even likely, that the effectiveness of seismo-electric coupling will decrease as TOC increases. Assuming that the main applications of seismo-electric methods will be in conventional, non-conventional and shale oil and gas plays, the dependence of the seismo-electric coupling on TOC is important.

We have carried out TOC measurements on our shale samples. All but two of our samples have a TOC in the range 3% to 5%, which makes them potential gas shales. The exceptional two samples had a low TOC, less than 1%. Figure 15c shows the seismo-electric coupling coefficient as a function of TOC. Considering samples with TOC>1% (i.e., those points in the box), the seismo-electric coupling coefficient is inversely proportional with respect to TOC, as hypothesised. At present the cause of the behaviour is not clear. It may be that the presence of kerogen either decreases the porosity of the sample or increases its tortuosity. Either of these effects will lead to a reduction in seismo-electric coupling, as indicated by Equation (6). Indeed, it is most likely that both effects occur because processes that tend to reduce the porosity of rocks also lead to their tortuosity increasing. It is also possible that the zeta potential is decreased for organically-rich shales. It has been observed that the zeta potential is diminished in organoclays due to the formation of inner-sphere complexes (Zacur et al. 2011, 2015).

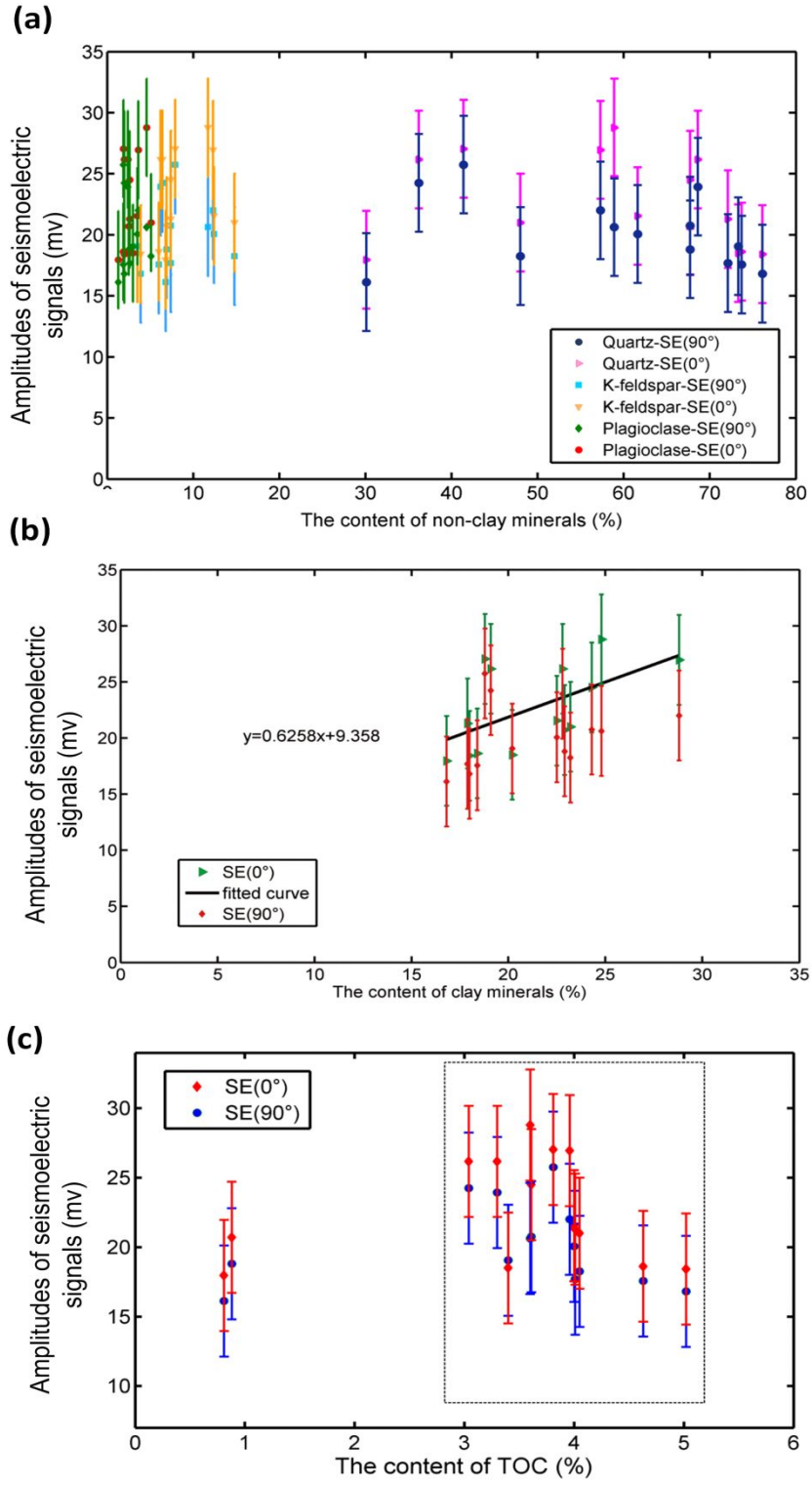

Figure 15. The amplitude of seismo-electric signals versus (a) the fraction of non-clay minerals (quartz, plagioclase, K-feldspar), (b) the fraction of clay minerals and (c) the fraction of TOC (total organic matter). The y-axis is the amplitudes of the seismo-electric signals measured by electrode V1. The measured data have error bars which are all about ±4 mV.

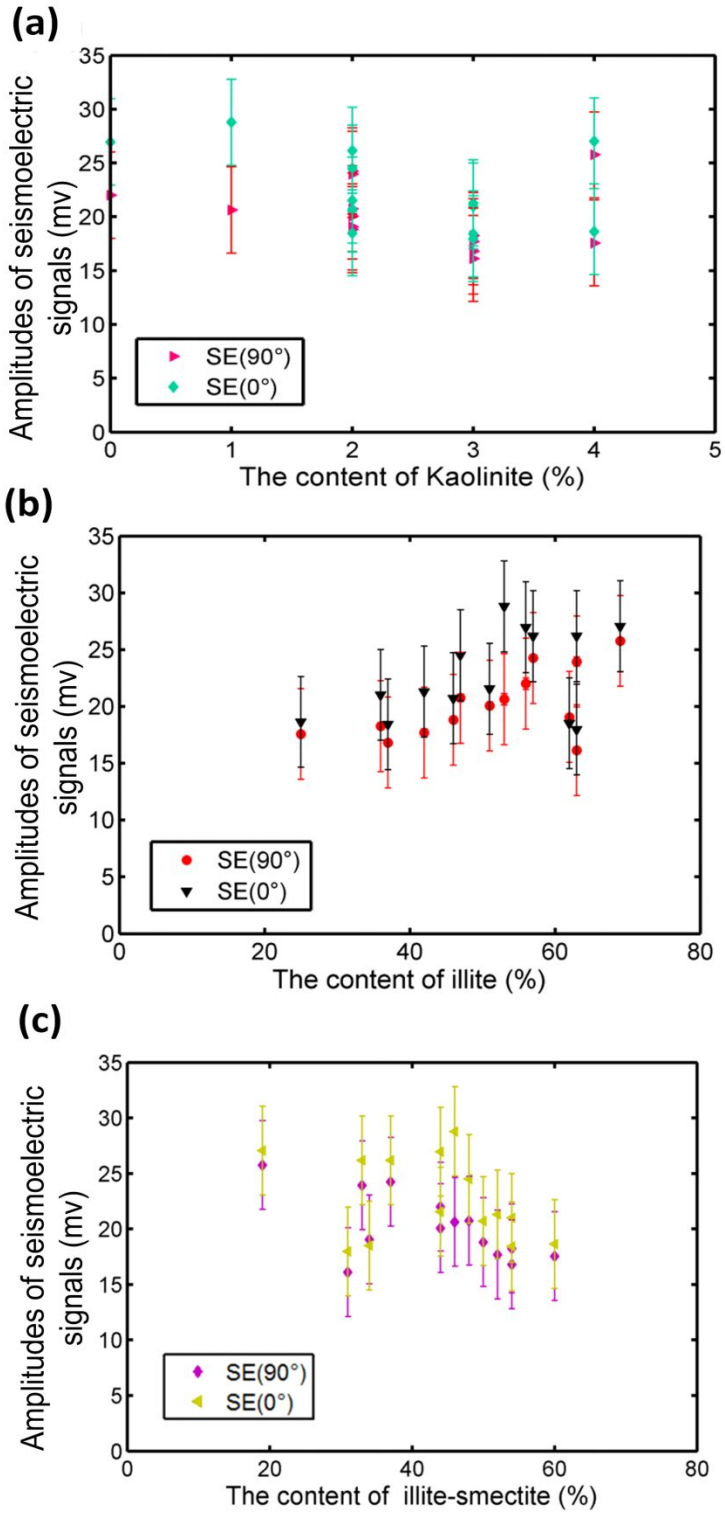

Figure 16. The influence of kaolinite, illite and illite/smectite mixed-layer on seismo-electric coupling. The *x*-axis is the percentage of minerals in the clay mineral. The y-axis is the amplitudes of the seismo-electric signals measured by electrode V1. The measured data have error bars which are all about ±4 mV. (a) Kaolinite, (b) Illite, and (c) Mixed Illite/Smectite.

8. Discussion

In this paper, we focused on what caused the strong seismo-electric conversion in low permeability shale and the influencing factors of seismo-electric conversion in shale.

We obtained the relationship between the seismo-electric conversion and clay minerals in shale, but the relationship in sandstones containing clay (shaly sand etc) need to be further studied. The increase of clay will increase the seismoelectric coupling coefficient. We think that no matter whether the clay is in shale or dispersed in sandstone, it will enhance seismo-electric conversion. Hence, the clay contents increase in sandstone will also increase the value of seismoelectric coupling. However, the relationships in shale and sandstones may be not the same. Because the structure of shale and sandstones are totally different, with shale having a much more anisotropic structure. In addition, the mineralogical components of sandstone and shale are different and will give rise to differences in the zeta potential. The zeta potential data of shale in the literature (Figure 13) is relatively small, so the empirical formula fitting out is not comprehensive. Proper zeta potential data of shale need to exclude the influence of surface conductivity, and the types of solutions should be the same, so there is not much data. Further work should carried out to both increase the size of the shale dataset and improve the seismo-electric model to include those aspects not included in the present model.

Further experimental measurements of seismo-electric conversion are needed. In this paper, we only examined NaCl solution as the experimental pore fluid. Further experiments changing the type of pore fluid (e.g., oil/water mixtures, pore fluids with different concentrations, saturations and compositions) may improve our knowledge of the fluid effects on seismo-electric conversion. In particular, experiments with multiphase pore fluids are needed to examine if it is possible to obtain seismo-electric signals induced at oil/water and gas/water interfaces; an ability which would help identify the oil/gas target and monitor its production using seismo-electric techniques. This paper reports seismo-electric anisotropy. A fuller study of this may provide parameters which are useful in characterizing the reservoir quality of the rock. This paper has also revealed a link between seismo-electric conversion, clay mineralogy and TOC, all of which need fuller study in order to fully characterize the processes that are occurring with the goal of using them to predict reservoir rock properties from remote seismo-electric measurements in the field.

We recognize that the experiments presented here can be improved upon. There would be a particular benefit in characterizing the experimental samples more fully, with additional measurements to determine the CEC and specific surface areas of the samples. Fuller analysis would be possible if the frequency-dependent complex conductivity of the samples were known such that phase lags, surface conductivities and the formation factors of the samples could be calculated. Also, the estimate of the tortuosity of the medium can also be obtained through the formation factor

(Clennell 1997; Jougnot et al. 2009), which will greatly reduce the uncertainty of influencing factors in this study. However, the samples have been used to measure other parameters after the seismoelectric measurements, such as TOC, test of shale elastic parameters and mineral component content tests, which had destroyed the samples, so we are not able to retrieve the conductivity data.

The relationship between the seismoelectric coupling and shale anisotropy need to gain a deep insight in future. In the comparison of numerical simulation and experimental results, the values of the seismoelectric coupling coefficients are the average value of parallel bedding and vertical bedding of shale, which is to simplify the result analysis. In fact, it is easy to find out from the results of this paper (Figure 5, Figure 15, Figure 16) that the amplitude of the seismoelectric signals of parallel bedding and vertical bedding are different. The signals' amplitudesof parallel bedding are larger than those of vertical bedding, which may be mainly related to the anisotropy of shale. Some may say it may be caused by the permeability anisotropy of shale, but we can see from the results of this paper that permeability is not the main factor that caused the strong seismo-electric conversion in shale. The permeability of shale in Sichuan Basin is less than 1 mD (Fu 2017). Comparing the curves below 1 mD (blue, orange and black curves) in Figure 10a, we can see that the three curves almost share the same seismo-electric value in a large range of frequency ($<10^6$ Hz). The seismo-electric conversion in the low permeability shale can be considered as a quasi-static behavior, there is little frequency dispersion, the seismo-electric conversion remains unchanged with the increasing frequency. Hence, the effect of permeability on seismo-electric conversion is not that great in shale, and the observed differences in seismoelectric signals measured parallel and perpendicular to bedding are not caused by the permeability anisotropy. That is to say, the difference of seismo-electric conversion in different directions of shale reflects the anisotropy of shale. We can call this phenomenon the seismo-electric anisotropy of shale. We all know that shale anisotropy can be reflected by elastic waves, while it is first proposed that shale anisotropy can be reflected by seismo-electric conversion. This needs to be confirmed and studied in detail.

Finally, we recognize that although much has been gained by comparing our experimental measurements with a model based on the Pride (1994) equation, that equation does not fully describe shales and that future work must expand the numerical model to include processes occurring in the Stern layer and which lead to Maxwell-Wagner and Interfacial polarization.

9. Conclusions

This paper investigates the characteristics of seismo-electric conversion in shales using experimental measurements and analytical modelling.

Experimental measurements have shown that the passage of acoustic waves through samples of sandstones and shales results in the generation of a seismoelectric voltage signal whose amplitude

and phase is a function of frequency and which can be characterized by a seismo-electric coupling coefficient. Experimental results show that the amplitude of the seismoelectric coupling coefficient in shales is comparable to that exhibited by sandstones. Furthermore, anisotropy which arises from bedding in the shales results in anisotropy in the amplitude of the seismoelectric signals.

Numerical modelling has been used to examine the effects of varying five parameters in the Pride (1994) model of seismo-electric conversion in porous media. The parameters investigated were (i) dimensionless number, (ii) porosity, (iii) permeability, (iv) tortuosity, and (v) zeta potential. Each of these parameters has different effects on the magnitude of the low frequency behaviour of the seismoelectric coupling coefficient and/or the frequency at which dispersive behaviour occurs as characterised by the critical frequency. While changes in dimensionless number and permeability seem to have little effect, seismoelectric coupling coefficient is highly sensitive to changes in porosity, tortuosity and zeta potential. Numerical modelling suggests that the cause of the seismo-electric conversion in shales, which otherwise have low porosities and permeabilities, is enhanced zeta potentials caused by clay minerals. Comparison of numerical modelling with the experimental data has supported that conclusion together with an analysis of seismo-electric conversion as a function of clay mineral composition.

Numerical modelling has also shown that the frequency-dependent behaviour can be safely ignored for most natural porous media because it occurs only at frequencies much higher than those encountered in conventional seismology (usually >10 kHz).

The sensitivity of seismo-electric coupling to the content of clay minerals and the TOC in shale suggests that seismo-electric exploration may have future potential for the characterization of clay minerals in conventional reservoirs as well as in characterising shale gas and shale oil reservoirs.

Acknowledgements

The authors would like to acknowledge the advice and help of Andre Revil, whose comments have greatly improved the paper. The study is supported by The Geological Survey Project of China Geological Survey (DD20190437), the China National Science & Technology Major Project (No. 2016ZX05007-006), China National Natural Science Foundation (41373036) and China National Key Research and Development Project (2016YFC0600209).

References

Alali, F., 2007. Dependence of NMR and SIP parameters on clay content, master's thesis, Berlin University of Technology.

Arulanandan, K., 1969. Hydraulic and electrical flows in clays, *Clays & Clay Minerals*, **17**(2), 63–76.

Bhattarcharyya, K.G. & Gupta, S.S., 2009, Adsorptive accumulation of Cd(II), Co(II), Cu(II), Pb(II) and Ni(II) ions from water onto Kaolinite: Influence of acid activation, *Adsorption Science and Technology*, **27**(1), 47-68.

Boudreau, B.P., 1996. The diffusive tortuosity of fine-grained unlithified sediments, *Geochimica Et Cosmochimica Acta*, **60**(16), 3139–3142.

Bruggeman, D.A.G., 1935. Berechnung verschiedener physikalischer Konstanten von heterogenen Substanzen. I. Dielektrizitätskonstanten und Leitfähigkeiten der Mischkörper aus isotropen Substanzen, *Ann. Phys*, **416** (7), 636–664.

Butler, K. E., Russell, R. D., Kepic, A. W. & Maxwell, M., 1996. Measurement of the seismo-electric response from a shallow boundary, *Geophysics*, **61**(6), 1769-1778.

Butler, K.E., Kepic, A.W. & Rosid, M.S., 2002. An experimental seismo-electric survey for groundwater exploration in the Australian outback, *SEG Technical Program Expanded Abstracts*, **21**(1), 1484.

Charlaix, E., Kushnick, A.P. & Stokes, J.P., 1988. Experimental study of dynamic permeability in porous media, *Physical Review Letters*, **61**(14), 1595-1598.

Chen, L., Zhang, L., Kang, Q., Yao, J. & Tao, W.Q., 2015. Nanoscale simulation of shale transport properties using the lattice Boltzmann method: permeability and diffusivity, *Sci Rep*, **5**, 8089.

Chorom, M. & Rengasamy, P., 1995. Dispersion and zeta potential of pure clays as related to net particle charge under varying ph, electrolyte concentration and cation type, *European Journal of Soil Science*, **46**(4), 657–665.

David, C., 1993. Geometry of flow paths for fluid transport in rocks, Journal of Geophysical research, **98**(B7), 12267-12278.

Debye, P. & Hückel E., 1923. Theory of electrolytes: I. lowering of freezing point and related phenomena, *Phys. Z*, **24**, 185-206.

Deng, J.X., Wang, H., Zhou, H, Liu, Z.H., Song, L.T. & Wang, X.B., 2015. Microtexture, seismic rock physical properties and modeling of Longmaxi Formation shale, *Chinese J. Geophy*., **58**(6), 2123–2136.

Dupuis, J.C., Butler, K.E., Kepic, A.W. & Harris, B.D., 2009. Anatomy of a seismo-electric conversion: measurements and conceptual modeling in boreholes penetrating a sandy aquifer, *Journal of Geophysical Research Solid Earth*, **114**(B10).

Epstein, N., 1989. On tortuosity and the tortuosity factor in flow and diffusion through porous media, *Chemical Engineering Science*, **44** (3), 777–779.

Fosu-Duah, E.L., Padmanabhan, E. & Gamez, V. J., 2016. Electrophoretic behavior of some shales from the Setap Formation, Sarawak Basin, Malaysia, *International Journal of Applied Engineering Research*, **11**, 337–341.

Fosu-Duah, E. L., Padmanabhan, E. & Gamez, V. J., 2017. Characteristic zeta potential of selected oligocene-Miocene shale from the Setap Formation onshore Sarawak-Malaysia, *International Journal of Applied Engineering Research.* **12**, 6360–6368.

Fu, C.Q., 2017. Study on Reservoir Characteristics and Shale Gas Enrichment of Wufeng-Longmaxi Formation Shale in Southeast Chongqing, Doctor's dissertation, China University of Mining and Technology, Beijing.

Jougnot, D., Revil, A. & Leroy, P., 2009. Diffusion of ionic tracers in the Callovo-Oxfordian clay-rock using the Donnan equilibrium model and the formation factor, *Geochimica et Cosmochimica Acta*, **73**(10), 2712–2726.

Jougnot, D., Revil, A., Lu, N. & Wayllace, A., 2011. Transport properties of the callovo-oxfordian clay rock under partially saturated conditions, *Water Resources Research*, **46**(8), 416–428.

Glover, P. W.J., 2009. What is the cementation exponent? A new interpretation. *Leading Edge* (Tulsa, OK), **28**(1). 82-85.

Glover, P.W.J., 2012. *Geophysical Properties of the Near Surface Earth: Electrical Properties*, Treatise on

Geophysics, Second Edition, pp. 89–137. Elsevier.

Glover, P.W.J. & Déry, N., 2010. Streaming potential coupling coefficient of quartz glass bead packs: Dependence on grain diameter, pore size, and pore throat radius, *Geophysics*, **75**(6), F225–F241.

Glover, P.W.J. & Jackson, M.D. (2010). Borehole electrokinetics, *The Leading Edge*, **29**(6), 724–728.

Glover, P.W.J., Walker, E., Ruel, J. & Tardif, E., 2012a. Frequency dependent streaming potential of porous media—Part 2: Experimental measurement of unconsolidated materials, *Int. J. Geophys*., **2012**, 1–17.

Glover, P.W.J., Walker, E. & Jackson, M.D., 2012b. Streaming-potential coefficient of reservoir rock: A theoretical model, *Geophysics*, **77**(2), D17–D43.

Haartsen, M.W. & Pride, S.R., 1997. Electroseismic waves from point sources in layered media, *J. Geophys. Res*., **102**(1022), 24745–24784.

Haines, S.H. & Pride, S.R., 2006. Seismo-electric numerical modeling on a grid, *Geophysics*, **71**(6), 57–65.

Haines, S.H., Pride, S.R., Klemperer, S.L. & Biondi, B., 2007. Seismo-electric imaging of shallow targets, *Geophysics*, **72**(2), G9–G20.

Johnson, D., Koplik, J. & Dashen, R., 1987. Theory of dynamic permeability and tortuosity in fluid-saturated porous media, *Journal of Fluid Mechanics*, **176**, 379–402.

Jouniaux, L. & Zyserman, F. I., 2016. A review on electrokinetically induced seismo-electrics, electro-seismics, and seismo-magnetics for Earth sciences, *Solid Earth*, **7**, 249–284.

Kitagawa, Y., Yorozu, Y. & Itami, K., 2001. Zeta potentials of clay minerals estimated by an electrokinetic sonic amplitude method and relation to their dispersibility, *Clay Sci*, **11**(4), 329–336.

Kozak, M.W. & Davis, E.J., 1989. Electrokinetics of concentrated suspensions and porous media: 2. moderately thick electrical double layers, *Journal of Colloid & Interface Science*, **129**(1), 166-174.

Kröger, B., Yaramanci, U. & Kemna, A., 2009. Modelling of seismo-electric effects, *The COMSOL Conference 2008, Hannover.*

Leroy, P. & Revil, A., 2004. A triple-layer model of the surface electrochemical properties of clay minerals, *Journal of Colloid and Interface Science*, 371-380.

Leroy, P. & Revil, A., 2009. A mechanistic model for the spectral induced polarization, *Journal of Geophysical Research*, **114**, B10202.

Leroy, P., Tournassat, C., Bernard, O., Devau, N. & Azaroual, M., 2015. The electrophoretic mobility of montmorillonite. Zeta potential and surface conductivity effects, *Journal of Colloid and Interface Science*, **451**, 21-39.

Liu, Z. C., Zhang, F. & Li, X. Y., 2019, Elastic anisotropy and its influencing factors in organic-rich marine shale of southern China, *Science China Earth Sciences*, **62**(11), 1805-1818.

Lu, S., Huang, W., Chen, F., Li, J., Wang, M., Xue, H., Wang, W. & Cai, X., 2012. Classification and evaluation criteria of shale oil and shale gas resources: Discussion and application, *Petrol. Explor. Dev.* **39**(2), 268-276.

Macht, F., Eusterhues, K., Pronk, G.J. & Totsche, K.U., 2011. Specific surface area of clay minerals: Comparison between atomic force microscopy measurements and bulk-gas (N2) and -liquid (EGME) adsorption methods, *Applied Clay Science*, **53**(1), 20-26.

Müller, R.H., 1996. Zeta potential und partikeladung in der laborpraxis, Dorctor's dissertation, Free University of Berlin, Berlin

Peng, R., Wei, J.X., Di, B.R., Ding, P.B. & Liu, Z.C., 2016. Experimental research on seismo-electric effects in

sandstone, *Applied Geophysics*, **13**(3), 425–436.

Peng, R., Di, B.R., Wei, J.X., Ding, P.B., Zhao, J., Pan, X. & Liu, Z.C., 2017. Experimental study of the seismo-electric interface response in wedge and cavity models, *Geophysical Journal International*, **210**, 1703–1720.

Peng, R., Glover, P.W.J., Di, B., Wei, J., Lorinczi, P., Ding, P. & Liu, Z., 2018a. The Effect of Rock Permeability and Porosity on Seismo-electric Conversion, *80th EAGE Conference and Exhibition 2018 Proceedings. Denmark.*

Peng, R., Di, B., Wei, J., Glover, P.W.J., Lorinczi, P., Ding, P. &Liu, Z., 2018b. The Seismo-electric Coupling in Shale, *80th EAGE Conference and Exhibition 2018 Proceedings. Denmark.*

Pride, S., 1994. Governing equations for the coupled electromagnetics and acoustics of porous media, *Physical Review B Condensed Matter*, **50**(21), 15678.

Pride, S. & Morgan, F. D., 1991. Electrokinetic dissipation induced by seismic waves, *Geophysics*, **56**(7): 914–925.

Revil, A. & Glover, P. W. J., 1997. Theory of ionic-surface electrical conduction in porous media, *Physical Review B - Condensed Matter and Materials Physics*, **55**(3), 1757–1773.

Revil, A. & Glover, P. W. J., 1998. Nature of surface electrical conductivity in natural sands, sandstones, and clays. *Geophysical Research Letters*, **25**(5), 691–694.

Revil, A., Pezard, P. A. & Glover, P. W. J., 1999a. Streaming potential in porous media: 1. theory of the zeta potential, *Journal of Geophysical Research Solid Earth*, **104**(B9), 20021–20031.

Revil, A., Schwaeger, H., Iii, L. M. C. & Manhardt, P. D., 1999b. Streaming potential in porous media: 2. theory and application to geothermal systems, *Journal of Geophysical Research Solid Earth*, **104**(B9), 20033–20048.

Revil, A., Leroy, P. & Titov, K., 2005. Characterization of transport properties of argillaceous sediments: Application to the Callovo-Oxfordian argillite, *Journal of Geophysical Research-Solid Earth*, **110**, B06202.

Revil, A., Jardani, A., Sava, P. & Haas, A., 2015. *The Seismo-electric Method: Theory and Application*. Wiley-Blackwell.

Rezaee, R. & Rothwell, M., 2015. Gas shale: Global significance, distribution and challenges, In *Fundamentals of Gas Shale Reservoirs*, First Edition, Ed. Reza Rezaee, John Wiley & Sons Inc.

Samyukta, K., Pashin, J. C., Ramsey, J. D. & Clark, P.E., 2017. Quantitative characterization of polyacrylamide–shale interaction under various saline conditions, *Petroleum Science*, **14**(3), 586–596.

Santiwong, S. R., Guan, J. & Waite, T. D., 2008. Effect of the ionic strength and pH on the hydraulic properties of accumulating solid assemblages during microfiltration of montmorillonite suspensions, *J. Colloid Interface Sci.*, **317**(1), 214– 227.

Saomoto, H. & Katagiri, J., 2015. Direct comparison of hydraulic tortuosity and electric tortuosity based on finite element analysis, *Theoretical and Applied Mechanics Letters*, **5**(5), 177-180.

Schakel, M. D., Smeulders, D. M. J., Slob, E. C. & Heller, H. K. J., 2011a. Laboratory measurements and theoretical modeling of seismo-electric interface response and coseismic wave fields, *J. Appl. Phys.*, **109**(7), 074903.

Schakel, M. D., Smeulders, D. M. J., Slob, E. C. & Heller, H. K. J., 2011b. Seismo-electric interface response: experimental results and forward model, *Geophysics*, **76**(4), N29–N36.

Shaw, D. J., 1992. *The solid-liquid interface, in Introduction to Colloid and Surface Chemistry*. 4th edn (pp. 151–173). Butterworth-Heinemann.

Thompson, A. H. & Gist, G. A., 1993. Geophysical applications of electrokinetic conversion, *The Leading Edge*,

12, 1169–1173.

Thompson, A. H., Hornbostel, S., Burns, J., Murray, T., Raschke, R. & Wride, J., et al., 2007. Field tests of electroseismic hydrocarbon detection, *Geophysics*, **72**(72), 565.

Tournassat, C., Chapron, Y., Leroy, P., Bizi, M. & Boulahya, F., 2009. Comparison of molecular dynamics simulations with triple layer and modified Gouy-Chapman models in a 0.1 M NaCl-montmorillonite system, *Journal of Colloid and Interface Science*, **339**(2), 533–541.

Tournassat, C., Grangeon, S., Leroy, P. & Giffaut, E., 2013. Modeling specific ph dependent sorption of divalent metals on montmorillonite surfaces. a review of pitfalls, recent achievements and current challenges, American Journal of Science, **313**(5), 395-451.

Walker, E. & Glover, P.W.J., 2010. Permeability models of porous media: Characteristic length scales, scaling constants and time-dependent electrokinetic coupling, *Geophysics*, **75**(6), E235–E246.

Walker, E., Glover, P.W.J. & Ruel, J., 2014. A transient method for measuring the DC streaming potential coefficient of porous and fractured rocks, *Journal of Geophysical Research: Solid Earth*, **119**, 957–970.

Walker, E. & Glover, P.W.J., 2018. Measurements of the relationship between microstructure, pH and the streaming and zeta potentials of sandstones, *Transport in Porous Media*, **121** (1). 183–206.

Wang, L., Chen, Y. & Liu Y., 2014. Shale Porous Structural Characteristics of Longmaxi Formation of Southeast Sichuan Basin, China Petroleum Exploration, **19**(5), 80-88.

Wang, J., Hu, H., Guan, W., 2015a, Experimental measurements of seismoelectric signals in borehole models, Geophys. J. Int., **203**(3): 1937–1945

Wang, J., Hu, H., Guan, W., Li, H., 2015b. Electrokinetic experimental study on saturated rock samples: zeta potential and surface conductance, *Geophys. J. Int.*, **201**(2): 869–877.

Wang, J., Hu, H. & Guan, W., 2016. The evaluation of rock permeability with streaming current measurements, *Geophys. J. Int*., **206** (3): 1563–1573.

Wang, J., Zhu, Z., Gao, Y. et al., 2020. Measurements of the seismoelectric responses in a synthetic porous rock. *Geophys. J. Int*. (under reviewing).

Xie, Q., Chen, Y., You, L., Hossain, M.M. & Saeedi, A., 2018. Drivers of wettability alteration for oil/brine/kaolinite system: implications for hydraulic fracturing fluids uptake in shale rocks, *Energies*, **11**(7), 1666.

Zacur S.S., Naranjo P.M. & Farfán, E.M., 2011. Organoarcillas: Propiedades electrocinéticas y estructura, Anales XVII Congreso Argentino de Físicoquímica, Córdoba, Argentina.

Zacur, S., Sham, E. & Torres, E.M.F., 2015. Measure of zeta potential of titanium pillared clays, *Procedia Materials Science*, **8**, 599–607.

Zhang, T. S., Yang, Y., Gong, Q. S., Liang, X., Wei, X. F., 2014, Characteristics and Mechanisms of the Micro-pores in the Early Marine Shale, Southern Sichuan Basin. *Acta Geologica Sinica*, **88**(9), 1728-1740.

Zhu, Z., Toksöz, M.N. & Burns, D.R., 2008. Electroseismic and seismo-electric measurements of rock samples in a water tank, *Geophysics*, **73**(5), E153–E164.

Zhu, Z. & Toksöz, M.N., 2013. Experimental measurements of the streaming potential and seismo-electric conversion in Berea sandstone, *Geophysical Prospecting*, **61**(3), 688–700.

Zhu, Z., Toksöz, M.N. & Zhan, X., 2015, Seismo-electric measurements in a porous quartz-sand sample with anisotropic permeability, *Geophysical Prospecting*, **64**(3), 700–713.

980